

# Application of a multiscale approach for modelling the rheology of complex fluids in industrial mixing equipment

F. De Roma,<sup>1</sup> D. Marchisio,<sup>1</sup> G. Boccardo,<sup>1</sup> M. Bouaifi,<sup>2</sup> and A. Buffo<sup>1, a)</sup>

<sup>1</sup>*DISAT, Institute of Chemical Engineering, Politecnico di Torino,  
C.so Duca degli Abruzzi 24, Torino 10129, Italy*

<sup>2</sup>*Centre de Recherche et d'Innovation de Lyon, Solvay, 85 Avenue des Frères Perret,  
BP 62, Saint-Fons Cedex 69192, France*

(Dated: 15 January 2024)

Many industrial sectors, like the personal care one, make wide use of mixing processes that involve complex fluids. However, modelling the rheology of these fluids is still challenging due to their non-Newtonian behaviour, which depends also on the local composition. Computational tools such as Dissipative Particle Dynamics (DPD) have been already used to calculate the equilibrium properties of these systems. Moreover, different works have been focused on the calculation of transport properties from these mesoscale DPD simulations. Multiscale approaches have been proposed to couple rheological information from DPD with Computational Fluid Dynamics (CFD) simulations. The CFD technique reproduces the macroscale piece of equipment, implementing a rheology model built using the Gaussian Process Regression (GPR), a mathematical tool related to machine learning. In this work, such framework is tested on an industrial process, to assess its performance on a realistic application. The investigated system is a solution at a high concentration of Sodium Lauryl Ether Sulfate (SLES) in water under laminar fluid dynamics regime. The results show that the mixture correctly exhibits a shear-thinning behaviour and presents viscosity values in good agreement with rheology experiments. While the feasibility of the coupling approach is shown, further studies on DPD are needed to improve the accuracy and the predictability of the methodology.

---

<sup>a)</sup> Author to whom the correspondence should be addressed: [antonio.buffo@polito.it](mailto:antonio.buffo@polito.it)

## I. INTRODUCTION

The personal care industry makes extensive use of ionic and non-ionic surfactants mixed with water for the production of everyday items, such as shampoos and soaps. Usually, the final products for the consumer market have low to moderate concentrations of surfactants ( $\sim 12 - 25\%$ )<sup>1,2</sup>. On the other hand, the semi-finished products present considerably higher concentrations of surfactants. Consequently, during the production step, a great variety of composition conditions are explored. In these blends, the concentration of surfactants plays a crucial role, due to their capability of undergoing self-assembly at the microscopic scale<sup>3</sup>. This process leads to the formation of different microstructures depending on composition, ranging from the micellar one to the hexagonal, cubic, and lamellar ones<sup>4,5</sup>. For this reason, these fluids are often referred to as structured fluids or complex fluids. The self-assembly occurs also in solutions of water and Sodium Lauryl Ether Sulfate (SLES)<sup>3-5</sup>, one of the most commonly used surfactants for personal care products. The presence of microstructures influences greatly the rheology of complex fluids, whose apparent viscosity depends on the composition and on the shear rate<sup>3,4</sup>. As a result, building a model for this rheological behaviour is considerably challenging and requires a significant amount of experimental data.

The continuous advances in the field of computational methods can be a great aid to the modelling process. Various simulation techniques allow the reproduction of the features of the fluids, from the microstructures at the mesoscale to the macroscopic fluid dynamics in the industrial equipment. In particular, Dissipative Particle Dynamics (DPD) is a computational technique that employs coarse-graining (CG) to describe the molecules in a fluid. The CG description leads to a reduction of the required computational resources when compared to other atomistic techniques, such as Molecular Dynamics (MD). This is due to the reduction of the degrees of freedom, which allows to explore higher spatial and temporal scales while retaining a certain degree of chemical specificity. The DPD technique has already been proven to be able to reproduce a variety of microstructures for complex fluids<sup>6,7</sup>. The parameterization of a DPD fluid is a vibrant field of study and various approaches were proposed over the years. Since the initial developments of the technique, Groot and Warren<sup>8</sup> built the parameter set for a simple fluid to match the compressibility of water. Moreover, they proposed a method based on Flory-Huggins theory of polymer solutions to derive the interaction parameters for systems with large molecules<sup>8</sup>. This approach found wide usage in the literature in numerous different applications, like surfactants in oil/water systems<sup>9</sup>,

phase diagrams for ternary mixtures<sup>6</sup> or polymer solutions<sup>10</sup>. An automated approach to build the coarse-grained model and identify the parameters was developed by Fraaije *et al.*<sup>11</sup> and recently tested on interfacial systems<sup>12,13</sup>. A parameterization method for small molecules based on fitting the partition coefficients in water-octanol was proposed by Anderson *et al.*<sup>14</sup>. The method produces a set of parameters that can be used for different molecules and has been already used to simulate alkyl surfactants. Among these, there was an interest in investigating the phase diagram for solutions of surfactants in water<sup>15</sup>, in calculating equilibrium properties<sup>16,17</sup> and the effect of cosurfactants<sup>18</sup>. These studies, though, analyzed low concentrations of alkyl surfactants in water, exploring only the typical final formulations for the consumer market. Moreover, they focused on equilibrium properties, leaving aside the calculation of transport properties, such as diffusion coefficients and viscosity. Nonetheless, since its development, DPD has been considered a promising tool for the evaluation of transport properties for colloidal systems<sup>19,20</sup> and polymer solutions<sup>21</sup>. Various methods have been employed to calculate the viscosity of a DPD fluid<sup>22</sup>. Simple fluids exhibit Newtonian behaviour, and their viscosity can be evaluated both with equilibrium<sup>23,24</sup> and non-equilibrium<sup>22</sup> techniques. On the other hand, non-equilibrium simulations are necessary to investigate shear-dependent rheology, typical of complex fluids<sup>7,25–27</sup>. These methods exhibit high uncertainty in viscosity values for low shear rate values<sup>25,28</sup> and bring to a rise in temperature and viscosity for high shear<sup>22</sup>, which is unphysical in many cases<sup>7</sup>. To have a better description of transport properties Junghans, Praprotnik, and Kremer<sup>29</sup> proposed a modification to the standard DPD thermostat, to include the effect of velocity components other than the radial one. For the same reason, increment of the dissipative coefficient  $\gamma$  was investigated<sup>22</sup> and *ad hoc* thermostats have been developed<sup>30,31</sup>.

While atomistic methods are helpful in calculating the properties of fluids, other techniques are instead suited to obtain useful information for design and optimization at the process scale. Among these, Computational Fluid Dynamics (CFD) has been used to simulate a great variety of applications, including mixing ones<sup>32,33</sup>. Hence, studies were already conducted on static mixers<sup>34–36</sup>, a piece of equipment often used to produce non-Newtonian solutions of surfactants in water.

Using the just described techniques, Zhao *et al.*<sup>37</sup> proposed a multiscale approach to simulate the behaviour of non-Newtonian fluids. The method uses DPD simulations to compute the viscosity of the fluid at different shear rates, generating a dataset used to build the rheology model. This latter step is performed using the Gaussian Process Regression (GPR), a mathematical and statistical tool that belongs to the family of machine learning techniques. The GPR is then directly

coupled with the CFD simulation, with the model that takes the shear rate values from the latter as input and gives the corresponding apparent viscosity in output. This multiscale approach was tested on a polymer melt<sup>37</sup> and on a diluted polymer solution<sup>38</sup> with promising results, but it was never applied directly to a realistic industrial process.

In this work, the rheological behavior of an industrial blend, made of a highly concentrated solution of SLES in water, is reproduced using an automated multiscale approach. The rheological information is extracted by means of a mesoscale DPD simulation and is used to build a rheology model. This is implemented through the GPR in a CFD simulation of the mixing equipment used for the blend production, *i.e.* an SMX static mixer. The DPD model of the fluid is successfully tested by a qualitative reproduction of the SLES/water phase diagram. The CFD is used to evaluate useful fluid dynamics details of the flow inside the static mixer together with the pressure drop across the device. The final values are plausible when compared with results obtained for similar blends in the same piece of equipment.

The next three sections are structured as follows: Section II illustrates thoroughly the methods and techniques used in this work, adding also information about the computational details. Section III reports and comments on the results, focusing on every step of the multiscale approach in different subsections. At last, the conclusions will be presented in Section IV.

## II. METHODS AND COMPUTATIONAL DETAILS

### A. The DPD technique

The first part of the multiscale approach consists in simulating the fluid at the mesoscale, to obtain information about its rheological behaviour. The technique used to perform these mesoscale simulations is the Dissipative Particle Dynamics (DPD), initially developed by Hoogerbrugge and Koelman<sup>39</sup> and later improved and formalized in detail by Español, Groot and Warren<sup>8,40</sup>. The DPD technique employs a coarse-grained description of the molecules, for which atoms are grouped together in particles called beads. These represent the fundamental elements in DPD simulations and can contain a number of atoms, or a number of molecules, depending on the desired level of coarse-graining (CG). As a consequence, DPD has the possibility to explore bigger scales in comparison to the full-atom Molecular Dynamics (MD) while keeping low the required computational resources.



The dynamics of the DPD particles can be described through Newton's equations of motion:

$$\frac{d\mathbf{r}_i}{dt} = \mathbf{v}_i, \quad (1a)$$

$$\frac{d\mathbf{v}_i}{dt} = \frac{\mathbf{f}_i}{m_i}, \quad (1b)$$

where  $\mathbf{r}_i$  is the position of the bead  $i$  with mass  $m_i$ , and  $\mathbf{v}_i$  is its velocity. In the standard DPD model of a simple fluid, the beads interact with each other through three pairwise forces, that are summed in the term  $\mathbf{f}_i$  of Eq. (1b):

$$\mathbf{f}_i = \sum_{i \neq j} (\mathbf{F}_{ij}^C + \mathbf{F}_{ij}^D + \mathbf{F}_{ij}^R). \quad (2)$$

These three forces regulate the interactions of two DPD beads up to a distance equal to the cut-off radius  $r_c$ . More in detail,  $\mathbf{F}^C$  is the conservative force:

$$\mathbf{F}_{ij}^C = \begin{cases} a_{ij} \left(1 - \frac{r_{ij}}{r_c}\right) \hat{\mathbf{r}}_{ij} & r_{ij} \leq r_c \\ 0 & r_{ij} > r_c \end{cases}, \quad (3)$$

which defines a soft repulsive potential, that allows beads to interpenetrate each other and even overlap. In this latter case, the conservative force reaches its maximum, which is equal to the repulsive parameter  $a_{ij}$ , whose value depends on the type of beads  $i$  and  $j$ . The distance between a pair of particles is identified with  $r_{ij} = |\mathbf{r}_{ij}| = |\mathbf{r}_i - \mathbf{r}_j|$  and  $\hat{\mathbf{r}}_{ij} = \mathbf{r}_{ij}/r_{ij}$  is the unit vector representing the direction that connects the centers of the two beads. The dissipative force  $\mathbf{F}_{ij}^D$  and the random force  $\mathbf{F}_{ij}^R$  have the following structure:

$$\mathbf{F}_{ij}^D = -\gamma w^D(r_{ij})(\mathbf{r}_{ij} \cdot \mathbf{v}_{ij}) \hat{\mathbf{r}}_{ij}, \quad (4)$$

$$\mathbf{F}_{ij}^R = \sigma w^R(r_{ij}) \frac{\xi_{ij}}{\sqrt{\Delta t}} \hat{\mathbf{r}}_{ij}, \quad (5)$$

where  $w^D(r_{ij})$  and  $w^R(r_{ij})$  are the weight functions,  $\mathbf{v}_{ij} = \mathbf{v}_i - \mathbf{v}_j$  is the relative velocity between two beads  $i$  and  $j$  and  $\xi_{ij}$  is a Gaussian white-noise variable with zero mean value and unit variance. These two forces act like a thermostat, in which  $\mathbf{F}^D$  is used to model viscous phenomena and  $\mathbf{F}^R$  is used to model the thermal agitation of the molecules. Español and Warren<sup>40</sup> showed that to respect the fluctuation-dissipation theorem the dissipative and random forces must be related, through the values of the parameters  $\gamma$  and  $\sigma$  and through their weight functions:

$$\sigma^2 = 2\gamma k_B T, \quad (6)$$

138

$$w^D(r_{ij}) = [w^R(r_{ij})]^2 = \begin{cases} \left(1 - \frac{r_{ij}}{r_c}\right)^2 & r_{ij} \leq r_c \\ 0 & r_{ij} > r_c \end{cases}. \quad (7)$$

139 These equations ensure the conservation of the energy in the system, in which the two forces act  
 140 properly as a thermostat. Moreover, the relation between  $\mathbf{F}^D$  and  $\mathbf{F}^R$  results in momentum con-  
 141 servation and correct hydrodynamic behavior of the DPD fluids for sufficiently large scales<sup>37,41</sup>.

142 Due to its coarse-grained nature, the DPD model is based on reduced units. It is possible to  
 143 retrieve the values in physical units from the DPD reduced units through the use of conversion  
 144 factors. The values of these factors depend on the coarse-graining level of the model, but their  
 145 identification for a given system is not trivial<sup>27</sup>. While some procedures were developed for equi-  
 146 librium simulations and simple fluids, in the case of non-equilibrium simulations it does not exist  
 147 a well-established methodology. The approach chosen for the work here presented is based on  
 148 matching the properties of interest for the systems studied. Hence, the conversion factors are  
 149 identified in order to match the viscosity of the system at a given shear rate:

$$\mu_{\text{cf}} = \frac{\mu}{\mu_{\text{DPD}}}, \quad (8a)$$

150

$$\dot{\gamma}_{\text{cf}} = \frac{\dot{\gamma}}{\dot{\gamma}_{\text{DPD}}}, \quad (8b)$$

151

$$\mathcal{E}_{\text{cf}} = \frac{\mathcal{E}}{\mathcal{E}_{\text{DPD}}} = \frac{k_B T}{k_{B,\text{DPD}} T_{\text{DPD}}}. \quad (8c)$$

152 In Eq. (8) the subscript “cf” indicates the conversion factor, while the values in DPD units are  
 153 marked with the subscript DPD, and the remaining quantities are expressed in physical units.  
 154 Defining also the conversion factor for a third quantity, in this case the energy in Eq. (8c), it is  
 155 possible to derive the conversion factor for any physical quantity. Considering that the standard  
 156 model of the DPD is isothermal, it was possible to establish the energy of the system starting from  
 157 a reference temperature.

## 158 B. Non-equilibrium simulations

159 To simulate a fluid under shear it is possible to apply the Lees-Edwards boundary conditions  
 160 (LEBC)<sup>42</sup>, which is used to obtain the velocity profile corresponding to the desired shear rate

inside a periodic box. The LEBC method was originally developed and widely used in the context of MD simulation, but its implementation has been already studied and used in conjunction with DPD in the past<sup>7,22,27</sup>. From such kind of simulation it is possible to obtain the pressure tensor  $\mathbf{P}$ , computed according to the following equation, in which  $i$  and  $j$  identify different beads:

$$\mathbf{P} = \frac{1}{V} \sum_{i=1}^N m_i \mathbf{v}_i \mathbf{v}_i + \frac{1}{V} \sum_{j>i}^N \sum_{i=1}^{N-1} \mathbf{r}_{ij} \mathbf{F}_{ij}^T. \quad (9)$$

The apparent viscosity of the DPD fluid can be calculated from the elements of the pressure tensor:

$$\mu = -\frac{P_{xy}}{\dot{\gamma}}, \quad (10)$$

where  $P_{xy}$  is the non-diagonal component of the pressure tensor relative to the plane in which the shear  $\dot{\gamma}$  is applied.

The DPD simulations were performed using the open-source software LAMMPS<sup>43</sup> (Large-scale Atomic/Molecular Massively Parallel Simulator). For non-equilibrium simulations, Lagrangian-Rhomboid boundary conditions (LRBC) are implemented in LAMMPS. The LRBC are equivalent to the LEBC as representation for a simple shear flow<sup>44,45</sup> and the main difference consists in how the shear is imposed. For  $\dot{\gamma} = \partial v_x / \partial y \neq 0$  using the LEBC, the shear is imposed using a “sliding brick” approach: the periodic images below and above the simulation box are displaced at  $\pm L \dot{\gamma} \Delta t$  in respect to the box itself. The position and velocity of the particles that cross the  $y$  boundaries are set in order to take into account the different values of  $v_x$  in the periodic images. Moreover, the interaction between two particles separated by a boundary is corrected to consider the displacement of the periodic boxes. To obtain the desired velocity profile using the LRBC instead, the box itself is deformed, as illustrated in Fig. 1, with a rate corresponding to the desired shear. The deformation induces a perturbation in the velocity of the DPD beads and under the condition of linear profile for the velocity within the simulation box, the Eq. (10) can be used to calculate the apparent viscosity.

In the approach here described an initial equilibrium simulation is conducted, in order to save the state of the DPD fluid that reached a dynamic equilibrium condition. This state can be used as a starting point since it allows to skip the repetition of the equilibration step for every non-equilibrium simulation. Consequently, the LRBC are directly applied to the equilibrated fluid in the box, imposing the desired shear rate. Due to the rise in temperature resulting from the imposition of the shear rate on the box, the SLLOD equations of motion were used, which in LAMMPS

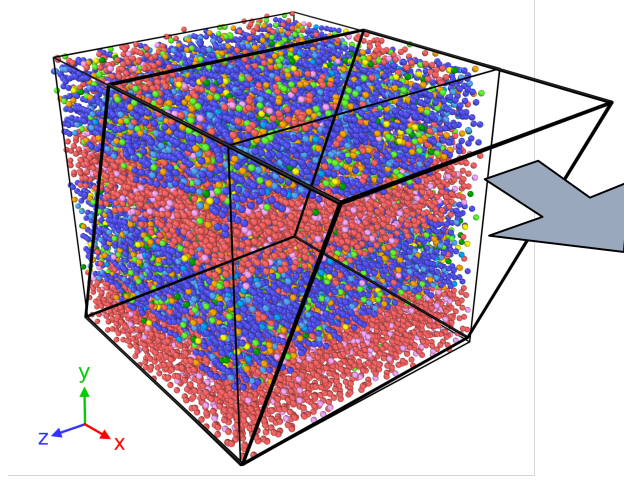


FIG. 1. Illustration of the deformation resulting from the imposition of the LRBC on a DPD box.

implement a Nose-Hoover thermostat. This approach is widely used in Molecular Dynamics<sup>44,45</sup>, and has been lately adopted in some works to perform non-equilibrium DPD simulation with shear<sup>46</sup>.

This paragraph reports the parameters that are common to all the DPD simulations of the present work. In particular, the value of numerical density for the beads is  $\rho_{\text{DPD}} = 3$  and all the bead types have unitary mass in DPD units. The simulation domain is a cubic box, with a side of length  $L = 40$  (DPD units) used to test the parameters (as described in Section III A) and one of length  $L = 20$  (DPD units) used to carry out the non-equilibrium simulations. The velocity-Verlet algorithm was used to integrate the equations of motion in all the DPD simulations with a timestep  $\Delta t = 0.01$  (DPD units).

### C. Miraspec UB75 model

The modeled fluid is the Miraspec UB75, a three-component mixture with composition reported in Table I.

Besides water, the table reports the use of other two main components:

- The Inter ESA-70 is a mixture of SLES (Sodium Lauryl Ether Sulfate) at 70% in water, whose main function is cleansing.
- CME/A2 is cocamide monoethanolamine (CMEA), used to control foaming, viscosity, and

TABLE I. Composition of the blend Miraspec UB75 used for the DPD simulations.

Component	Mass fraction
Inter ESA-70	0.72
CME/A2	0.08
Water	0.20

mildness of the product.

As depicted in Fig. 2 and Fig. 3, both SLES and CMEA have an alkyl tail, which can be formed by a different number of carbon atoms. In particular in Table II and Table III are reported the percentages of the molecules for every length of the alkyl chain. These characterize the components of the blend and they are used to calculate the numerical concentrations of the beads in the DPD simulations of the Miraspec UB75.

TABLE II. Percentage of SLES molecules with a specific length of the alkyl chain, expressed in number of carbon atoms, in the Inter ESA-70 component.

Number of Carbon atoms	Percentage in Inter ESA-70
12	70%
14	30%

TABLE III. Percentage of CMEA molecules with a specific length of the alkyl chain, expressed in number of carbon atoms, in the CME/A2 component.

Number of Carbon atoms	Percentage in CME/A2
8	6%
10	6%
12	50%
14	18%
16	9%
18	11%

Again in Fig. 2, it is shown that the SLES molecule can have a different number of ethoxyl (EO)

212 groups  $(\text{CH}_2\text{CH}_2\text{O})_n$ . While the Miraspec UB75 contains only molecules of SLES with a single  
 213 EO group, the phase diagram reported in the work of Li *et al.*<sup>3</sup> refers to SLES molecules with  
 214 three EO groups. Consequently, the molecule used for the validation in Section III A contained  
 215 two more  $[\text{CH}_2\text{OCH}_2]$  beads than the one depicted in Fig. 2.

216 The process of developing the final model went through different steps. Initially, a DPD model  
 217 for SLES and water is tested, using the set of parameters to reproduce the phase diagram of the  
 218 mixture. Then a coarse-grained model for CMEA is developed with the same parametrization  
 219 method, and the correct reproduction of the microstructure of the blend is used as a test. In the  
 220 end, the non-equilibrium simulations are performed with the developed DPD model, to obtain the  
 221 information on the rheology of the fluid. It must be remarked that it does not exist a unique stan-  
 222 dardized process to develop the parameters of a DPD model. Hence, depending on the system  
 223 features and the level of coarse-graining, different methods can be used. Anderson *et al.*<sup>14</sup> devel-  
 224 oped a parametrization scheme based on the water-octanol partition coefficients. The parameters  
 225 obtained with this technique have been used to simulate micellar blends of alkyl sulfate, alkyl  
 226 ethoxylate and alkyl ethoxy sulfate surfactants<sup>14–18</sup>. In this work we used the latter approach to  
 227 model the SLES molecules, adopting the same CG level depicted in Fig. 2.

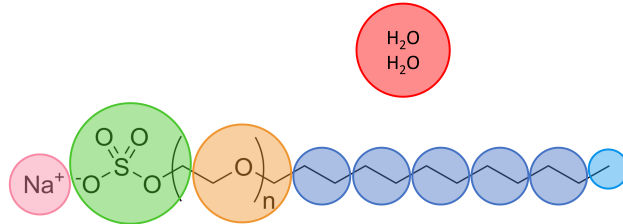


FIG. 2. Coarse graining model adopted for water and SLES molecules<sup>15</sup>. Changing the length of the alkyl tail results in the addition or the subtraction of  $[\text{CH}_2\text{CH}_2]$  beads.

228 The full list of conservative parameters  $a_{ij}$  and cutoff radii  $r_{c,ij}$ , reported in Table IV, was  
 229 obtained from previous works<sup>14,15</sup>, while in Table V are reported the dissipative parameters  $\gamma$  and  
 230 the stochastic one  $\sigma$ , common to all the beads.

TABLE IV: List of conservative repulsive parameter  $a_{ij}$  and cutoff radius  $r_{c,ij}$  for each pair of beads.

Bead $i$	Bead $j$	conservative coefficient $a_{ij}$	cutoff radius $r_{c,ij}$
[H <sub>2</sub> O]	[H <sub>2</sub> O]	25.0	1.000
[CH <sub>3</sub> ]	[CH <sub>3</sub> ]	24.0	0.955
[CH <sub>2</sub> CH <sub>2</sub> ]	[CH <sub>2</sub> CH <sub>2</sub> ]	22.0	1.074
[CH <sub>2</sub> OCH <sub>2</sub> ]	[CH <sub>2</sub> OCH <sub>2</sub> ]	25.5	1.116
[CH <sub>2</sub> OSO <sub>3</sub> <sup>-</sup> ]	[CH <sub>2</sub> OSO <sub>3</sub> <sup>-</sup> ]	13.30	1.234
[Na]	[Na]	25.00	1.000
[CH <sub>3</sub> CH <sub>2</sub> ]	[CH <sub>3</sub> CH <sub>2</sub> ]	22.00	1.098
[CH <sub>2</sub> CONHCH <sub>2</sub> ]	[CH <sub>2</sub> CONHCH <sub>2</sub> ]	22.00	1.218
[CH <sub>2</sub> OH]	[CH <sub>2</sub> OH]	14.00	0.980
[H <sub>2</sub> O]	[CH <sub>3</sub> ]	45.00	0.977
[H <sub>2</sub> O]	[CH <sub>2</sub> CH <sub>2</sub> ]	45.00	1.037
[H <sub>2</sub> O]	[CH <sub>3</sub> ]	24.00	1.058
[H <sub>2</sub> O]	[CH <sub>2</sub> OCH <sub>2</sub> ]	17.90	1.117
[H <sub>2</sub> O]	[CH <sub>2</sub> OSO <sub>3</sub> <sup>-</sup> ]	25.00	1.000
[H <sub>2</sub> O]	[Na]	45.00	1.049
[H <sub>2</sub> O]	[CH <sub>3</sub> CH <sub>2</sub> ]	19.00	1.109
[H <sub>2</sub> O]	[CH <sub>2</sub> OH]	14.50	0.990
[CH <sub>3</sub> ]	[CH <sub>2</sub> CH <sub>2</sub> ]	23.00	1.014
[CH <sub>3</sub> ]	[CH <sub>2</sub> OCH <sub>2</sub> ]	28.50	1.020
[CH <sub>3</sub> ]	[CH <sub>2</sub> OSO <sub>3</sub> <sup>-</sup> ]	28.50	1.071
[CH <sub>3</sub> ]	[Na]	45.00	0.962
[CH <sub>3</sub> ]	[CH <sub>3</sub> CH <sub>2</sub> ]	23.00	1.026
[CH <sub>3</sub> ]	[CH <sub>2</sub> CONHCH <sub>2</sub> ]	32.00	1.086
[CH <sub>3</sub> ]	[CH <sub>2</sub> OH]	26.00	0.967
[CH <sub>2</sub> CH <sub>2</sub> ]	[CH <sub>2</sub> OCH <sub>2</sub> ]	28.50	1.095
[CH <sub>2</sub> CH <sub>2</sub> ]	[CH <sub>2</sub> OSO <sub>3</sub> <sup>-</sup> ]	28.50	1.154
[CH <sub>2</sub> CH <sub>2</sub> ]	[Na]	45.50	1.037



Table IV (continued): List of conservative repulsive parameter  $a_{ij}$  and cutoff radius  $r_{c,ij}$  for each pair of beads.

Bead $i$	Bead $j$	conservative coefficient $a_{ij}$	cut-off radius $r_{c,ij}$
[CH <sub>2</sub> CH <sub>2</sub> ]	[CH <sub>3</sub> CH <sub>2</sub> ]	22.00	1.086
[CH <sub>2</sub> CH <sub>2</sub> ]	[CH <sub>2</sub> CONHCH <sub>2</sub> ]	32.00	1.146
[CH <sub>2</sub> CH <sub>2</sub> ]	[CH <sub>2</sub> OH]	26.00	1.027
[CH <sub>2</sub> OCH <sub>2</sub> ]	[CH <sub>2</sub> OSO <sub>3</sub> <sup>-</sup> ]	15.50	1.175
[CH <sub>2</sub> OCH <sub>2</sub> ]	[Na]	24.00	1.058
[CH <sub>2</sub> OCH <sub>2</sub> ]	[CH <sub>3</sub> CH <sub>2</sub> ]	28.50	1.107
[CH <sub>2</sub> OCH <sub>2</sub> ]	[CH <sub>2</sub> CONHCH <sub>2</sub> ]	15.73	1.167
[CH <sub>2</sub> OCH <sub>2</sub> ]	[CH <sub>2</sub> OH]	25.00	1.059
[CH <sub>2</sub> OSO <sub>3</sub> <sup>-</sup> ]	[Na]	17.90	1.117
[CH <sub>2</sub> OSO <sub>3</sub> <sup>-</sup> ]	[CH <sub>3</sub> CH <sub>2</sub> ]	28.50	1.166
[CH <sub>2</sub> OSO <sub>3</sub> <sup>-</sup> ]	[CH <sub>2</sub> CONHCH <sub>2</sub> ]	13.57	1.226
[CH <sub>2</sub> OSO <sub>3</sub> <sup>-</sup> ]	[CH <sub>2</sub> OH]	21.70	1.048
[Na]	[CH <sub>3</sub> CH <sub>2</sub> ]	45.00	1.049
[Na]	[CH <sub>2</sub> CONHCH <sub>2</sub> ]	18.33	1.109
[Na]	[CH <sub>2</sub> OH]	25.80	0.990
[CH <sub>3</sub> CH <sub>2</sub> ]	[CH <sub>2</sub> CONHCH <sub>2</sub> ]	32.00	1.158
[CH <sub>3</sub> CH <sub>2</sub> ]	[CH <sub>2</sub> OH]	26.00	1.038
[CH <sub>2</sub> CONHCH <sub>2</sub> ]	[CH <sub>2</sub> OH]	26.00	1.099

TABLE V. DPD parameter in common to every bead of the Miraspec UB75 blend.

Parameter	Value (DPD units)
$\gamma$	10.125
$\sigma$	4.5

231 The bonded interactions between two consecutive beads are modeled using the harmonic po-  
232 tential in Eq. (11),

$$E_{\text{bond}} = \frac{1}{2}k_{\text{bond}}(r - r_0)^2, \quad (11)$$

with  $k_{\text{bond}} = 150$  (DPD units) for all the bonds and an equilibrium distance calculated according to the following equation<sup>16</sup>:

$$r_0 = 0.1(n_i + n_j) - 0.01 , \quad (12)$$

where  $n_i$  and  $n_j$  are the number of heavy atoms linearly bonded in the  $i$  and  $j$  bead respectively. According to this rule,  $n_i = 4$  for the sulfate bead, with two oxygen atoms that are considered “branched” from the linear chain. The model also includes an angle harmonic potential, that involves three beads interacting according to the formula:

$$E_{\text{angle}} = \frac{1}{2}k_{\text{angle}}(\theta - \theta_0)^2 , \quad (13)$$

where  $\theta$  is the angle between two adjacent bonds,  $k_{\text{angle}} = 5$  (DPD units) and  $\theta_0 = 180^\circ$  for all the interactions.

Within the model, it is particularly interesting the treatment of the charged beads, *i.e.* sodium ion and sulfate group. The standard DPD model allows overlapping of the beads, but in the case of  $r_{ij} = 0$  the Coulombic potential diverges, leading to the creation of artificial ionic pairs<sup>47,48</sup>. Previous works on analogous systems adopted a smeared charge approach to overcome this issue<sup>15–18</sup>. The same approach was kept in this work, using a Slater-type charge smearing formulated by González-Melchor *et al.*<sup>48</sup>:

$$E_{\text{el}} = \frac{Cq_iq_j}{\epsilon_r} \left( 1 - \left( 1 + \frac{r_{ij}}{\lambda} \exp(-2r_{ij}/\lambda) \right) \right) \quad r_{ij} \leq r_{c,\text{el}} , \quad (14)$$

where, following the implementation of Anderson *et al.*<sup>16</sup>, the decay length is  $\lambda = 1/0.929$  (DPD units) and  $r_{c,\text{el}} = 3$  (DPD units). The latter parameter,  $r_{c,\text{el}}$ , acts like a cutoff for the treatment of the electrostatic forces. When  $r_{ij} \leq r_{c,\text{el}}$  the interaction between two beads is evaluated through Eq. (14), while for  $r_{ij} > r_{c,\text{el}}$  the PPPM (particle-particle particle-mesh) solver, in its LAMMPS implementation, is used to evaluate the electric field. The previous literature focused on the study of solutions of SLES in water in micellar phases, a microstructure formed for low concentrations of the surfactant. Consequently, in these previous studies, the value of the dielectric permittivity constant was set equal to the one of water,  $\epsilon_r = 78.3$ . In the case of the Miraspec UB75, the concentration of the SLES is substantially higher, hence the value  $\epsilon_r = 25$  was used. This latter value was chosen because it allowed to reproduce qualitatively the microstructures for different compositions of the mixture of water and SLES, as reported in Section III A.

258 To simulate the CMEA molecules, a new CG representation was developed, as illustrated in  
 259 Fig. 3.

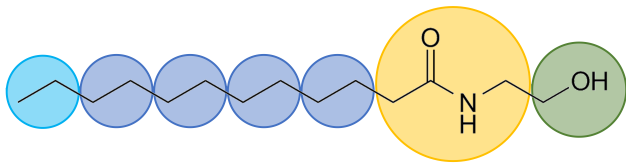


FIG. 3. Coarse graining model developed for CMEA molecules. Changing the length of the alkyl tail results in the addition or the subtraction of  $[\text{CH}_2\text{CH}_2]$  beads.

260 The DPD interaction parameters for the beads constituting the CMEA are only in part already  
 261 present in the literature, in the work of Wand *et al.*<sup>18</sup>; the rest were obtained using the same  
 262 approach, the water/octanol partition method<sup>14</sup>, and they were kindly provided by Dr. Richard  
 263 Anderson. These parameters are relative to the interactions of the  $[\text{CH}_2\text{OH}]$  bead present in the  
 264 CMEA molecule and are also listed in Table IV.

265 The set of conversion factors in Table VI was used for the UB75 blend and it comes from  
 266 matching one experimental value of viscosity. This approach was chosen due to the current im-  
 267 possibility of matching all the properties of a fluid with a single set of conversion factors in DPD.  
 268 This becomes particularly true for transport properties and when performing non-equilibrium sim-  
 269 ulations. In this case, a linear velocity profile must be obtained in a small box, so the stream  
 270 velocity must overcome the thermal velocity of the beads. Together with the nature of the DPD  
 271 forces, this leads to very high shear rates at the macroscale and may result in a shift of the rheol-  
 272 ogy model. Hence, the identification of conversion factors focused on matching the properties of  
 273 interest, *i.e.* viscosity and shear rate, also intending to compensate for the described shift to higher  
 274 shear rates. From the available experiments, the viscosity at the lowest shear rate was matched  
 275 with the lowest meaningful value of the DPD shear rate. This corresponds to the lowest  $\dot{\gamma}_{\text{DPD}}$  that  
 276 still results in a linear velocity profile from the imposition of the LRBC. For what concerns the en-  
 278 ergy conversion factor, it was obtained considering the temperature  $T = 298.15$  K, the Boltzmann  
 279 constant  $k_B = 1.38 \times 10^{-23} \text{ J} \cdot \text{K}^{-1}$ ,  $T_{\text{DPD}} = 1$ ,  $k_B = 1$  with the application of Eq. (8).

280 The equilibration stage lasted  $1.2 \times 10^6$  timesteps, while the deformation of the non-equilibrium

TABLE VI. Set of conversion factors used for the Miraspec UB75 DPD model.

$\mu_{\text{cf}} (\text{Pa} \cdot \text{s})$	$\dot{\gamma}_{\text{cf}} (\text{s}^{-1})$	$\mathcal{E}_{\text{cf}} (\text{J})$
2.59	10	$4.11 \times 10^{-21}$

stage was set to  $10^6$  timesteps. The cumulative average of the DPD viscosity is computed, and its value at the end of the simulation is extracted.

## D. Gaussian Process Regression

Although the information derived from Dissipative Particle Dynamic simulations is needed to reproduce the behavior of the fluid at the macroscale, a tight coupling between DPD and CFD is unfeasible. In such a coupling, the main hindrance would be the computational effort required to run microscale simulations. For this reason, the development of a kriging strategy to provide an unbiased rheological relationship is devised. A similar approach was proposed by Zhao *et al.*<sup>37</sup>, who used Gaussian Process Regression (GPR)<sup>49</sup> to link the viscosity values extracted from DPD with the imposed local shear rate. GPR is a mathematical and statistical tool akin to machine learning and to grasp the concept behind it, it is possible to think of a distribution over functions. When there are no training data points, the *prior distribution* is usually a distribution of functions whose mean is equal to zero and whose standard deviation is unitary. Indeed, for every value of the independent variable  $x$ , the value of  $y$  is normally distributed around a mean, with an associated standard deviation. Hence, it is important to stress that the GPR does not output a functional form of the target function, and it is instead a statistical model that outputs the predicted  $y$  values for any tested  $x$  in input. The shape of the functions sampled from this distribution derives from the Kernel, which defines the properties, such as derivability, of the mentioned functions. In this work a Radial Basis Function (RBF), or *squared exponential*, Kernel was used:

$$K(x_i, x_j) = \sigma_f^2 \exp \left( -\frac{d(x_i, x_j)^2}{2l^2} \right), \quad (15)$$

where  $\sigma_f$  is the *signal variance*, a pre-factor related to how much the functions vary vertically,  $d(\cdot, \cdot)$  is the Euclidian distance between the two points  $x_i$  and  $x_j$ , and  $l$  is the *characteristic length-scale*<sup>49</sup>. The latter parameter expresses how the functions can vary: a high value of  $l$  will output smoother functions, that do not show rapid variations. Often  $\sigma_f$  and  $l$  are referred to as *hyper-*

parameters since they are free parameters, whose value can be varied and it is usually optimized through different techniques.

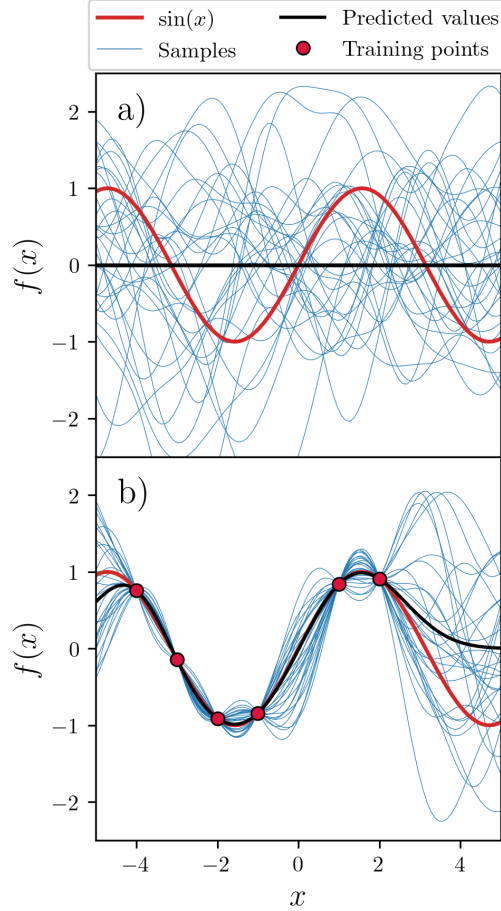


FIG. 4. Result of the GPR on an example function  $y = \sin(x)$  with RBF kernel. Different steps are illustrated: a) prior distribution, b) posterior distribution obtained with six training data points. The functions in blue are samples from the distributions of functions.

The addition of training points  $(x_{\text{train}}, y_{\text{train}})$  to the training data set changes the distribution of functions, which results in the *posterior distribution*. The effect of adding training data points can be noticed by comparing Fig. 4.a and Fig. 4.b, whose plots illustrate the use of the GPR on a test function  $y = \sin(x)$ . Considering the distribution of functions of a GPR model, it is possible to take samples from this distribution, analogously to what can be done by sampling a distribution of numbers. However, in this case, the samples correspond to functions that respect the constraints imposed by the used kernel and the training data set. Starting from the prior distribution in Fig. 4.a,

in which sample functions from the distribution are plotted in blue, the addition of training points forces said functions to pass through them, as in Fig. 4.b. The prediction values, plotted in black, are the result of the regression and they are generated by calculating the mean of the normally distributed functions.

Due to the width of the shear rate intervals, the GPR for the simulated systems was performed on the log-space, *i.e.* using the values of  $\log(\dot{\gamma})$  vs  $\log(\mu)$ , with an approach comparable to the one of Zhao *et al.*<sup>37</sup>.

In this work, the Python module *scikit-learn*<sup>50</sup> was used to perform the GPR step, and in particular to optimize the values of the hyperparameters  $\sigma_f$  and  $l$ . After the evaluation of the quality of the regression, the training data set and the values of the hyperparameter are passed to a GPR viscosity model implemented in the CFD code OpenFOAM. This viscosity model works as a function: after reading the GPR hyperparameters, it requires the local value of the strain rate, which is evaluated through the solution of the momentum balance equation, and it provides the viscosity value as output for each cell of the computational domain. The implementation of the GPR in OpenFOAM is written in C++ and it is inspired by freely available implementations on Github<sup>51</sup>.

## E. The CFD model

The last step of the multiscale approach is the Computational Fluid Dynamics (CFD) simulation, which makes use of the GPR viscosity model derived from the DPD non-equilibrium simulations. As previously mentioned, the CFD simulation can provide information about the fluid dynamics of mixing devices<sup>36,52</sup>. In this work, this simulation is carried out in isothermal conditions, under laminar regimen, and the fluid is considered incompressible. In this attempt to apply the multiscale approach to a complex fluid to test the feasibility, the concentration of the species in the system was considered uniform. As a consequence, the viscosity of the fluid depends only on the strain rate  $\dot{\gamma}$ , and the system is investigated at the steady state.

The CFD simulations were carried out using the software OpenFOAM (version 8)<sup>53</sup> and in particular the steady-state solver `simpleFoam`. The pressure-velocity coupling algorithm adopted is the SIMPLEC (consistent SIMPLE).

## F. Multiscale coupling

A linking step between the techniques described in the previous sections was developed, to build a functional and automated multiscale approach. The coupling is based on an iterative flow scheme, implemented in Python, reported in Fig. 5, with an approach similar to the one described in Zhao *et al.* <sup>37</sup>.

The starting point, as in Fig. 5, is a CFD simulation that implements a Newtonian model. The viscosity value for this Newtonian model can be obtained from an initial DPD simulation, performed with a low value of the shear rate  $\dot{\gamma}_{\text{DPD}}$ . With the completion of this first CFD simulation, the loop indicated with the blue arrows in Fig. 5 is initiated. This will be called *outer loop*, and it starts with the extraction of the interval of the strain rate values from the CFD simulation. The strain rate interval is then passed to the GPR, which builds the model from the training data set, *i.e.* the couples of points  $(\dot{\gamma}, \mu(\dot{\gamma}))$  obtained from the DPD simulations. Once the model is built, it takes the strain rate values in input and outputs the corresponding viscosity values (predictions) together with an associated standard deviation  $\sigma$ . This latter variable is then used to test the quality of the model in the whole interval. If the  $\sigma$  associated with any viscosity prediction is higher than a user-set limit  $\sigma_{\text{lim}}$ , the quality of the model is deemed not sufficient. In this case, the *inner loop*, indicated with the orange arrows in Fig. 5, starts and a new DPD simulation is issued. The value of  $\dot{\gamma}_{\text{DPD}}$  to impose for this simulation is the one corresponding to the maximum value of  $\sigma$  obtained in the tested interval. This iterative process is repeated until the regression is satisfactory, and a new training data point is added for every cycle of the loop. This makes the algorithm automated, since a certain number of DPD simulations are launched until the desired accuracy on the shape of the constitutive relationship is met. When the exit condition for the *inner loop* is respected, the GPR is implemented in OpenFOAM as a viscosity model, and a new CFD simulation is launched. The updated strain rate interval, extracted from the last simulation, is compared with the one previously fed to the GPR. If the new interval is wider than a tolerance set by the user, the GPR model is tested on the updated interval and the *inner loop* may start again, depending on the values of  $\sigma$ . The difference between the extremes of the shear rate intervals is calculated as a relative difference according to the following equations:

$$\epsilon_{\text{min,rel}} = \frac{\dot{\gamma}_{\text{min}}^{(n-1)} - \dot{\gamma}_{\text{min}}^{(n)}}{\dot{\gamma}_{\text{min}}^{(n-1)}}, \quad (16a)$$



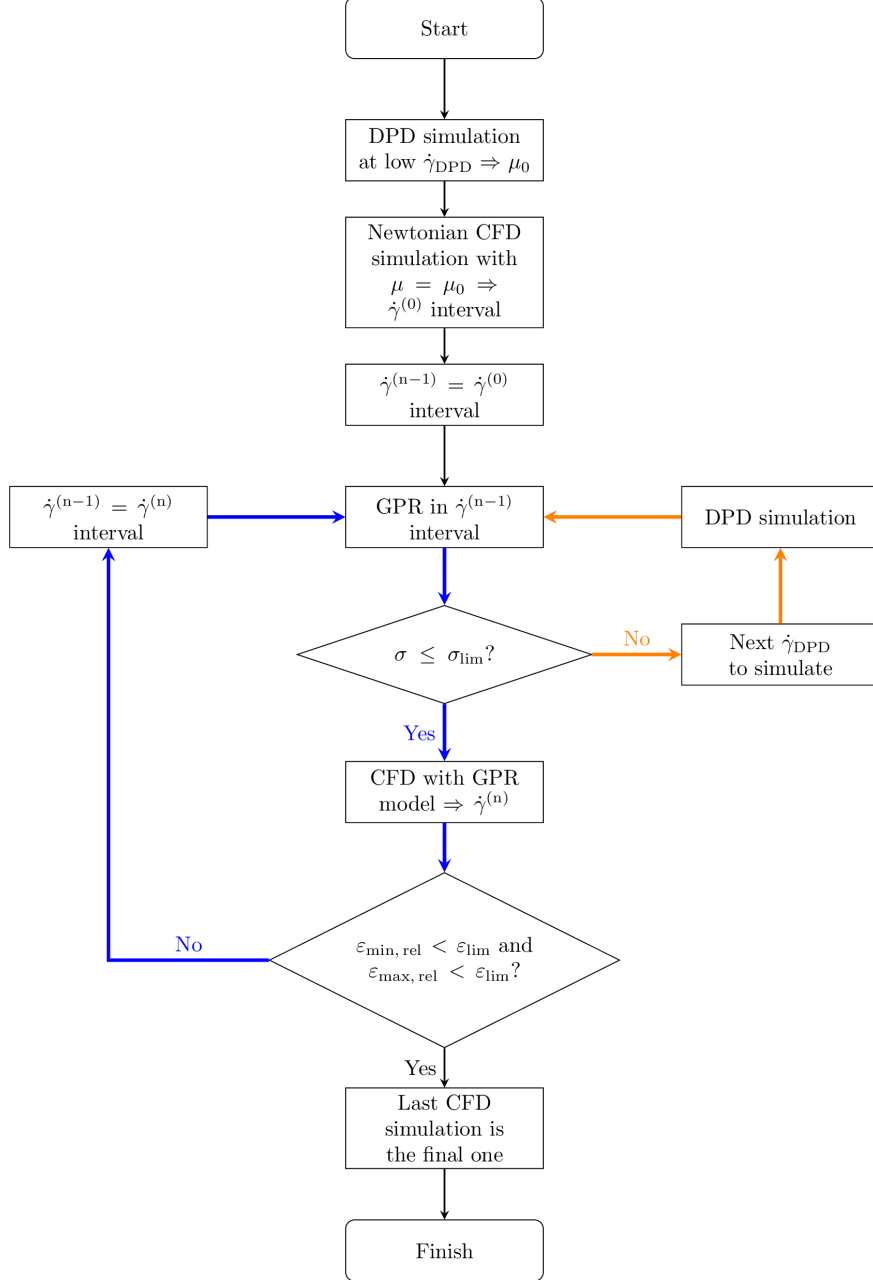


FIG. 5. Flowscheme used in the multiscale coupled approach. The following symbols are used:  $\dot{\gamma}_{DPD}$  is the shear rate used for a DPD simulation,  $\mu_0$  is the viscosity obtained from the first DPD simulation, and used to perform the Newtonian CFD simulation,  $\dot{\gamma}^{(i)}$  identifies the  $i$ -th rate interval from CFD simulations,  $\sigma$  is the standard deviation associated with the regression,  $\sigma_{lim}$  is the user-set limit for said standard deviation,  $\epsilon_{.,rel}$  is the relative difference between the extremes of two shear rate intervals as in Eq. (16), and  $\epsilon_{lim}$  is the user-set limit for said relative differences.

$$\varepsilon_{\max, \text{rel}} = \frac{\dot{\gamma}_{\max}^{(n)} - \dot{\gamma}_{\max}^{(n-1)}}{\dot{\gamma}_{\max}^{(n-1)}}, \quad (16b)$$

where  $\varepsilon_{\max, \text{rel}}$  and  $\varepsilon_{\min, \text{rel}}$  must be smaller than a set limit value  $\varepsilon_{\text{lim}}$  to exit the loop. It must be stressed that the absolute value is not used in Eq. (16) because the convergence criterion should discriminate between a wider and a narrower interval. The use of the absolute value will not lead to convergence in case of a much narrower  $\dot{\gamma}^{(n)}$  interval, since it would not take into account the sign of  $\varepsilon_{\max, \text{rel}}$  and  $\varepsilon_{\min, \text{rel}}$ . For this reason, the order of the terms at the numerator of Eq. (16) is of paramount importance. Conversely, if the interval is not significantly wider or the quality of the regression is sufficient, the process exits from the *outer loop*. At this point, the CFD simulation that was performed last is considered to be the one that reproduces the studied system.

### G. Sulzer SMX static mixer model

The application example selected in this work to test the multiscale coupling procedure is one step of the production process of the Miraspec UB75, namely the post-mixing section of a blend reported in Table I. This phase is carried in a static mixer, like the Sulzer SMX, that consists of a tube filled with mixing elements. Depending on the kind of application, these internal elements can have different shapes. In the studied equipment there are six identical mixing elements, each one rotated by 90° axis with respect to the previous, having the  $z$  axis as the axis of rotation. Every element is constituted by inclined bars, as it is possible to notice from Fig. 6. The inclination of each bar, with respect to both the main flux direction and the adjacent bars, is responsible for the mixing itself. The main flow gets broken down following smaller flow paths which are subsequently recombined due to the peculiar geometry of the mixer internals. Still in Fig. 6 is also displayed an initial empty region of the tube, used to obtain a developed flow at the beginning of the mixing section. The details of the static mixer geometry are reported in Table VII.

The boundary conditions applied to the system are summarised in Table VIII, where the pressure outlet value was kept at zero. The mesh is completely tetrahedral and contains 5118292 cells, and it has been selected after a grid convergence study. Based on the typical densities of these blends,  $\rho = 1160 \text{ kg m}^{-3}$  was imposed for the CFD simulations.

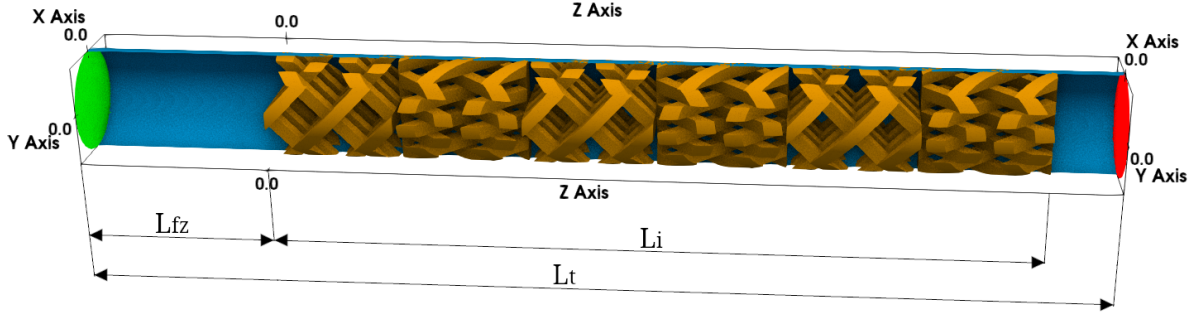


FIG. 6. Geometry of the SMX Sulzer static mixer used in the simulations. The color scheme identifies different regions of the geometry: green for the inlet, red for the outlet, blue for the wall of the tube, and orange for the mixing elements. This color coding is adopted for clarity, but in the actual computational domain used for the simulations the tube (blue) and the internals (orange) are part of the same wall patch, as in Table VIII.

TABLE VII. Geometrical details of the computational domain.

		Symbol	Value
Diameter	(mm)	$D$	16
Tube length	(mm)	$L_t$	160
Internals length	(mm)	$L_i$	122
Number of elements		$N_e$	6
Number of bars per element		$N_b$	4
Initial free zone length	(mm)	$L_{fz}$	30

### III. RESULTS AND DISCUSSION

#### A. Solvay's UB75 blend: testing the DPD model

Before showing the results obtained by the multiscale approach, it is worth to discuss specifically the DPD model and in particular the CG approach reliability. As previously mentioned, among many available approaches to build a DPD model for a large molecule, in this work we used the approach of Anderson *et al.*<sup>14</sup> to build the DPD model of the molecules in the Miraspec UB75 blend<sup>14,16</sup>. The starting point is the Inter ESA-70, a mixture of Sodium Lauryl Ether Sulfate (SLES) molecules with different lengths of the alkyl tail. The coarse-grained model of a SLES

TABLE VIII. Boundary conditions used for the CFD simulations with the SMX Sulzer.

	Wall	Inlet	Outlet
		Fixed value	
Velocity	No slip	$U_x, U_y = 0$ $U_z = 1.38 \times 10^{-2} \text{ m s}^{-1}$	Zero gradient
Pressure	Zero gradient	Zero gradient	Fixed value $p = 0 \text{ Pa}$

molecule and the DPD parameters reported in Ref. 15 were tested. The DPD model assessment is carried out through a qualitative comparison between simulation results and the experimental phase diagram of a SLES/water mixture<sup>3</sup>. It is important to notice that the mixture reproduced to test the parameters does not exactly represent the Inter ESA-70. More precisely, the SLES molecules simulated in this step present a higher number of ethoxyl groups and a different length of the alkyl chain<sup>3</sup>. Nonetheless, the ability to reproduce a water/SLES phase diagram can provide a measure of the quality of the DPD model for these kinds of molecules. The lower side of the ternary phase diagram in Ref. 3 represents a binary mixture of SLES and water, from which three regions are identified to conduct the assessment. While for low SLES concentrations (0.00236 – 28% w/w) a micellar phase is found, intermediate SLES concentrations (31.5 – 56% w/w) lead to the formation of the hexagonal phase and for high SLES concentrations (63 – 70% w/w) a transition to lamellar phase occurs<sup>4</sup>.

One equilibrium DPD simulation in each of these regions is performed, and the resulting microstructure is qualitatively analyzed. The three DPD simulations performed are summed up in Table IX, and they resulted in agreement with the phase diagram, as it is possible to see in Fig. 7.

TABLE IX. Values of SLES mass fraction used in the DPD simulation and corresponding expected microstructure according to Refs. 3 and 4.

Expected structure	Simulated SLES mass fraction
Micellar	0.03
Hexagonal	0.45
Lamellar	0.67

417 In particular, to obtain a qualitative confirmation of the hexagonal structure, it was necessary  
 418 to conduct a non-equilibrium simulation with an imposed shear rate  $\dot{\gamma} = 0.1$  (DPD units) on the  
 419 velocity component  $v_x$  along the  $y$  axis. This kind of behavior was already reported in the literature  
 420 for a DPD model that simulates a mixture of water and a tri-block co-polymer<sup>7</sup>. When there is  
 421 no shear applied the fluids form a network of worm-like micelles, as in Fig. 7.c. From Fig. 7.d  
 422 it is clear how the application of a shear brings to the formation of rodlike micelles, typical of  
 423 hexagonal structures.

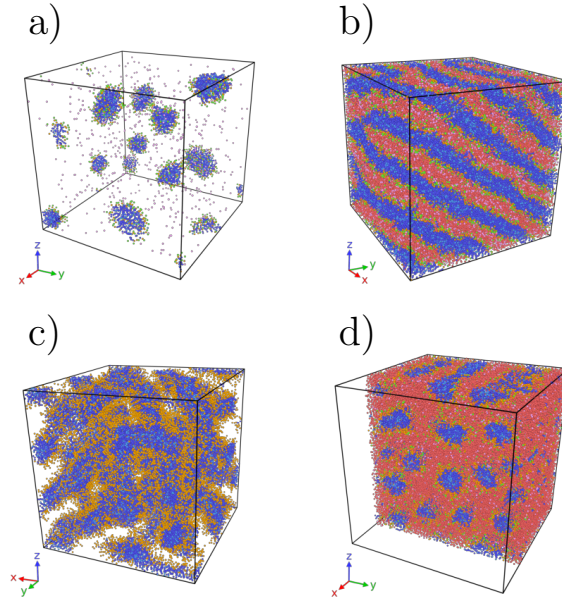


FIG. 7. Resulting microstructures of the DPD simulation performed. SLES mass fraction equal to a) 0.03,  
 b) 0.67, c) and d) 0.45. In c) there is no shear applied, the water and the sulfate groups beads are not  
 shown to highlight the network formed by the wormlike micelles, while in d) the system is shown after the  
 application of a shear of  $\dot{\gamma} = 0.1$  (DPD units) along the  $y$  axis to the velocity component  $v_x$ . To allow the  
 micelles visualization, the water beads are not shown in a). To facilitate the visualization of the rodlike  
 micelles in d) the box is sliced at  $3/4$  of its length in the  $x$  direction. The color coding of the beads is shown  
 in Fig. 2.

424 Having assessed the qualitative capability of the model to predict the microstructure self-  
 425 assembly for the binary system made of SLES and water, the addition of the third component  
 426 was tested. The CME/A2 component is Cocamide Monoethanolamine (CMEA), whose coarse-  
 427 grained model was developed and as described in Section II C with parameters for the DPD forces  
 428 retrieved from the literature<sup>14–16</sup>. In Fig. 8 it is shown that, for the composition in Table I, it is

429 obtained a lamellar microstructure, which is indeed expected for the Miraspec UB75.

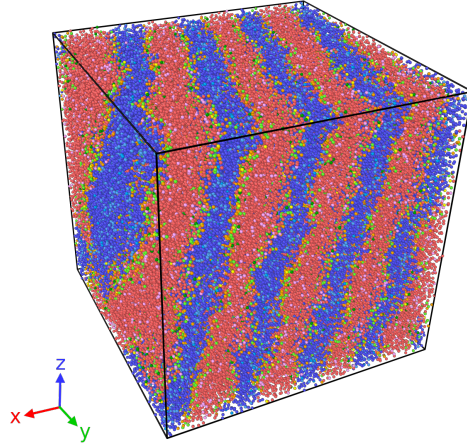


FIG. 8. Lamellar microstructure obtained from a simulation of the blend Miraspec UB75 with composition reported in Table I. The color coding of the beads is shown in Fig. 2 and Fig. 3.

## 430 B. Miraspec UB75 blend: pressure drops in Sulzer SMX

### 431 1. Multiscale approach and GPR

432 Once the performance of the DPD model for Miraspec UB75, described in detail in Section II C,  
433 was assessed, it was then used to simulate a more realistic macroscopic application. The produc-  
434 tion of this blend requires the usage of a static mixer, in which the components are mixed in  
435 multiple steps at various temperatures. The multiscale approach is here applied to a simplified  
436 version of the production process, isothermal and with uniform composition. The latter is a strong  
437 assumption, equal to having the blend already mixed at the entrance of the equipment. Besides  
438 the general performances of the multiscale approach, the macroscopic variable of interest is the  
439 pressure drop across the mixer.

440 Table X summarize the CFD simulations performed, using an incremental Roman number ev-  
441 ery time that an updated GPR model is used. As it is possible to see from this table, three CFD  
442 simulations were issued before the whole approach could reach convergence. The criterion here  
443 described refers to what, in the multiscale approach, is called *outer loop*, as expressed in Sec-  
444 tion II F. To evaluate the convergence of the iterative process, the strain rate interval extracted  
445 from a CFD simulation was compared with the one extracted from the previous simulation. The

TABLE X. Maximum and minimum value of the strain rate  $\dot{\gamma}$  inside the CFD domain with the different viscosity models. The variable  $\varepsilon$  is the difference, calculated as relative difference, between the values of one CFD run and the previous.

CFD run	$\dot{\gamma}_{\min} \times 10^{-2} (\text{s}^{-1})$	$\varepsilon_{\min, \text{rel}}$	$\dot{\gamma}_{\max} (\text{s}^{-1})$	$\varepsilon_{\max, \text{rel}}$
Newtonian	3.606		324.98	
GPR I	2.513	0.303	432.30	0.330
GPR II	2.488	0.010	361.05	-0.165

convergence criterion is set on the maximum ( $\dot{\gamma}_{\max}$ ) and on the minimum ( $\dot{\gamma}_{\min}$ ) values of the strain rate intervals, as follows:

$$\varepsilon_{\min, \text{rel}} = \frac{\dot{\gamma}_{\min}^{(n-1)} - \dot{\gamma}_{\min}^{(n)}}{\dot{\gamma}_{\min}^{(n-1)}} \leq 0.01, \quad (17a)$$

$$\varepsilon_{\max, \text{rel}} = \frac{\dot{\gamma}_{\max}^{(n)} - \dot{\gamma}_{\max}^{(n-1)}}{\dot{\gamma}_{\max}^{(n-1)}} \leq 0.01, \quad (17b)$$

where the superscript  $(n)$  refers to the latest CFD simulation and the superscript  $(n-1)$  refers to the previous CFD simulation. If the strain rate interval of the last CFD simulation is wider than 1% with respect to the one from the previous simulation, the GPR should test the training data on the newly extracted interval. One should notice that the condition is tested separately for the upper limit and the lower limit, and both need to be satisfied for convergence.

Fig. 9 shows the regression process applied to the first shear rate interval, which is extracted from the CFD simulation with the Newtonian viscosity model. Besides the rheograms, Fig. 9 depicts also information about the quality of the regression for the GPR loop, called *inner loop* in the multiscale approach (Section II F). As it is possible to see from Fig. 9.a2 and Fig. 9.b2, to reach the convergence of the GPR, the following equation must be satisfied in the whole strain rate interval:

$$\sigma \leq \sigma_{\text{lim}} = 10^{-2} \quad (18)$$

with  $\sigma_{\text{lim}}$  corresponding to the dotted orange line in the plots. Fig. 9.a1 and Fig. 9.a2 report the results of an incomplete GPR viscosity model, obtained with a partial training data set of two  $(\dot{\gamma}, \mu(\dot{\gamma}))$  couple of points. Fig. 9.b1 and Fig. 9.b2, instead, illustrate the viscosity model GPR I (Table X), obtained after the convergence of the GPR on the interval extracted from the Newtonian CFD simulation. Comparing Fig. 9.a1 and Fig. 9.b1 it is possible to illustrate how the addition of



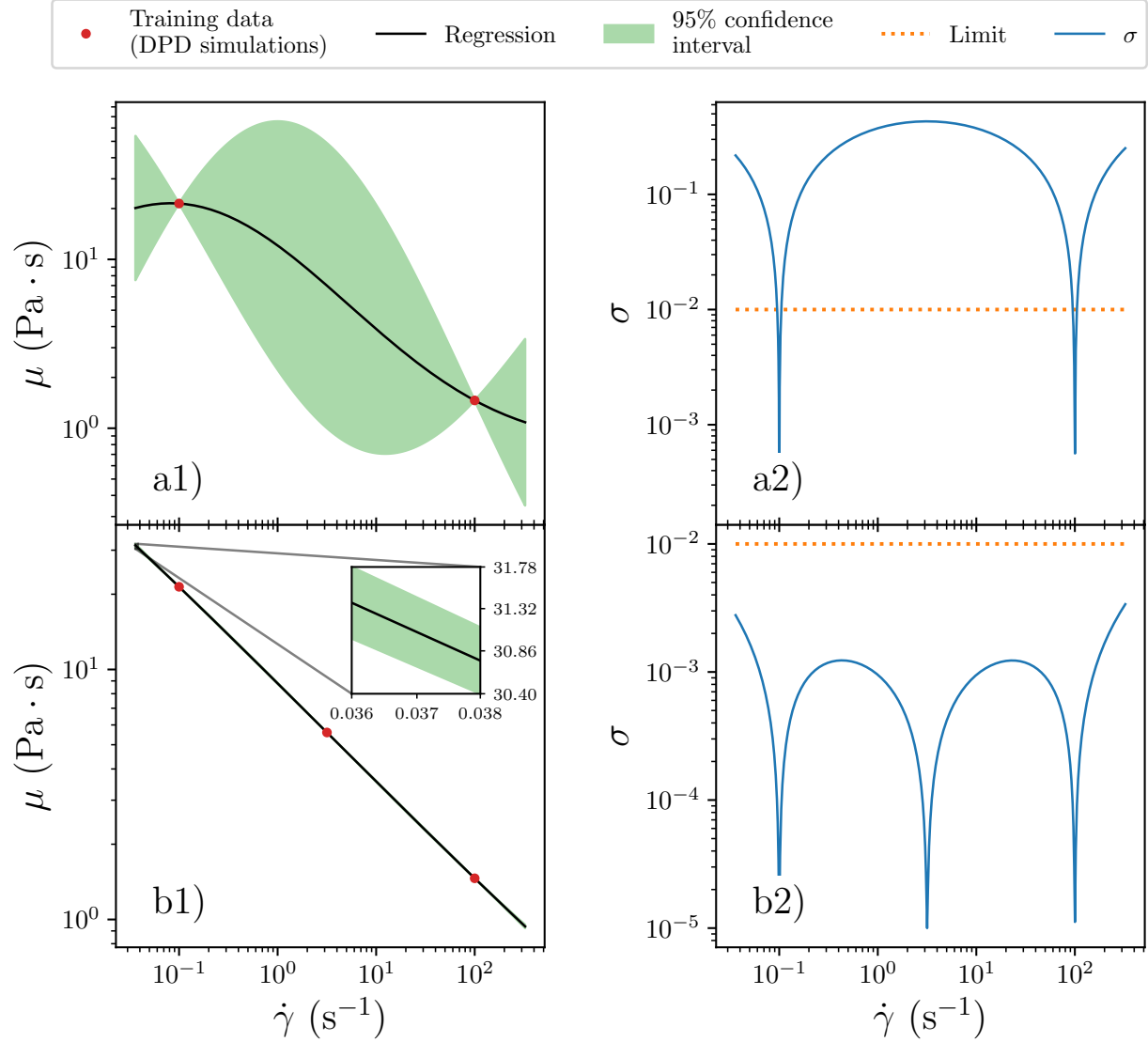


FIG. 9. Illustration of the regression process to build the viscosity model GPR I, using the shear rate interval extracted from the Newtonian CFD simulation. The different plots show: a1) rheogram of the incomplete GPR I model before convergence, a2) standard deviation associated to the regression of the incomplete GPR I model before convergence, b1) rheogram of the converged GPR I model, b2) standard deviation associated to regression of the converged GPR I model. The inset in b1) contains the magnification of a portion of the regression, to allow the visualization of the narrow 95% confidence interval.

the third data point to the data set substantially improves the regression. This is confirmed by the low values of  $\sigma$  shown in Fig. 9.b2, which correspond to a very narrow 95% confidence interval in Fig. 9.a2, as visible only in the magnified inset.

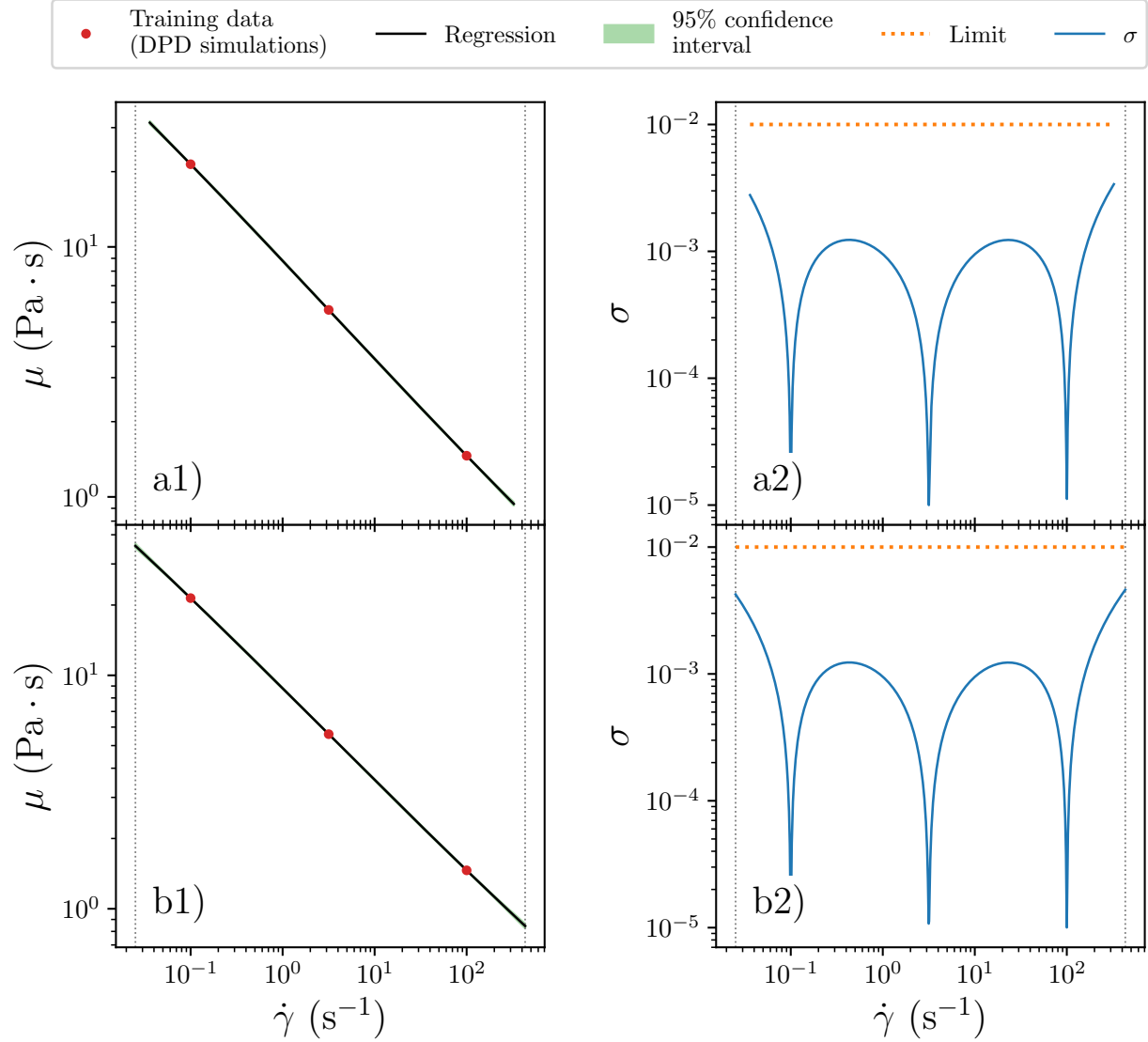


FIG. 10. Comparison between GPR I and GPR II viscosity model. The plots show: a1) rheogram of the converged GPR I model, a2) standard deviation associated to the regression of the converged GPR I model, b1) converged GPR II model, b2) standard deviation associated to the regression of the converged GPR II model. The 95% confidence intervals in a1) and b1) are slightly visible only close the the extremes of the curves, due to their narrowness. The dotted grey vertical lines highlight the different width between the intervals used for the regression in the two models.

The GPR I and GPR II viscosity models (Table X) are depicted in figure Fig. 10.a and Fig. 10.b respectively. As previously stated, the GPR I model is built on the shear rate interval extracted from the first CFD simulation, which employed a Newtonian viscosity model. The GPR II model

is instead built on the shear rate interval extracted from the second CFD simulation, which implemented the GPR I model. Moreover, the training data set used is the same for the two viscosity models, indicating that no additional DPD simulations were necessary to reach the convergence of the regression step. Consequently, the two viscosity models are very similar and the only difference resides in the shear rate interval. Indeed, the GPR II is built on a wider interval, as emphasized by the dotted vertical grey lines in Fig. 10. The 95% confidence intervals in Fig. 10.a1 and Fig. 10.b1 are very narrow and slightly visible only close to the extremes of the intervals. Hence,  $\sigma$  reaches its maxima in correspondence to the interval extremes in both Fig. 10.a2 and Fig. 10.b2, since the GPR technique performs worse in extrapolating than in interpolating. A third GPR viscosity model was not built since, as reported in Table X, the difference between the last  $\dot{\gamma}$  interval and the previous one respected the convergence criteria in Eq. (17). The difference between the limits of the strain rate intervals is also noticeable in Fig. 11, where the cumulative distribution functions of  $\dot{\gamma}$  are plotted. The same figure also shows that the  $\dot{\gamma}$  distributions for the two GPR models are basically superimposed, and the differences with the Newtonian one are not so relevant. The reason for such small differences is probably due to the viscosity value  $\nu$  used for the Newtonian simulation. The initial guess for the value of  $\nu$  resulted to be intermediate when compared with the extreme values of the final viscosity interval (Fig. 14.a). This could explain both the slight shift to higher  $\dot{\gamma}$  values of the Newtonian distribution and the different shape for intermediate values of strain rate.

A total of three DPD simulations were necessary during the whole process, to have the Eq. (18) respected, as illustrated by the series labeled as “Training data” in Fig. 9 and Fig. 10. The final viscosity model obtained with the multiscale approach is of a shear-thinning fluid. This is consistent with the experimental measures available, that usually lead to a power-law viscosity model for simulation purposes.

## 2. CFD simulations

The results of the CFD simulations are analyzed qualitatively through contour plots on the slice shown in Fig. 12. In this figure, it is reported the Slice  $\mathcal{A}$ , that cuts the domain with the plane  $x = 0$  m from the inlet section to the outlet one. In Fig. 13 the just described slice is used to compare the strain rate  $\dot{\gamma}$  inside the domain from different simulations. In these contour plots, it is shown that the strain rate trend in the domain is similar regardless of the viscosity model used.

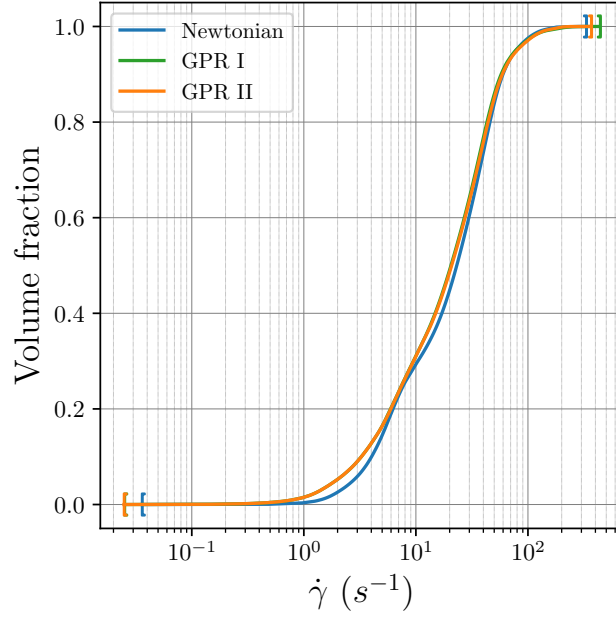


FIG. 11. Volume cumulative distribution function for the shear rate values in the different CFD simulations. The “[” and “]” markers correspond to the  $\dot{\gamma}_{\min}$  and  $\dot{\gamma}_{\max}$  respectively, for every interval.

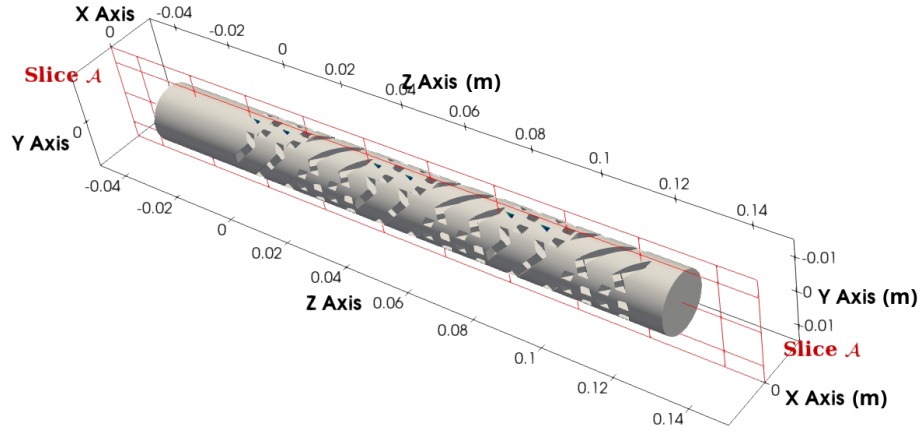


FIG. 12. Visual representation of the slice  $\mathcal{A}$  used for contour plots. This cuts the CFD domain with the plane  $x = 0$  m. All the lengths in the figure are expressed in meters.

501 The strain rate values are higher close to the walls of the tube and close to the mixing elements,  
502 while regions of low strain rates are found mostly at the inlet and outlet. Hence, the contour for the

503  $\dot{\gamma}$  is in a qualitative agreement with the theory since a steeper variation of the velocity of the fluid  
 504 is expected in correspondence with the walls. The only visible differences in the contour plots  
 505 are confined to the inlet region in the simulation with the Newtonian model. This is due to the  
 506 viscosity value of the fluid in that region, lower than the one in the non-Newtonian simulations,  
 507 which consequently influences the distribution of  $\dot{\gamma}$

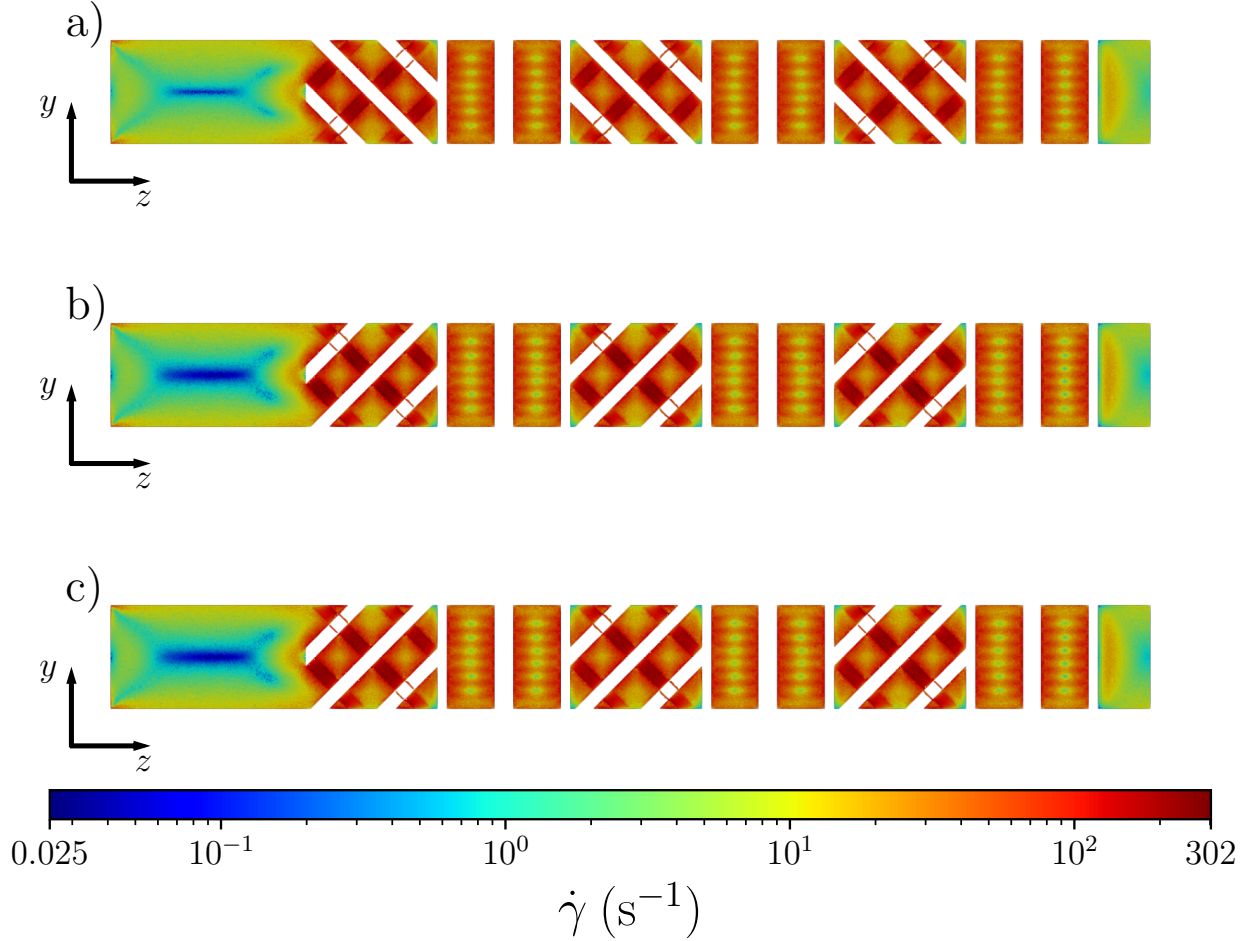


FIG. 13. Contour plot for the strain rate  $\dot{\gamma}$  in correspondence of the slice  $\mathcal{A}$ . The values are plotted using a logarithmic scale for the colorbar. Different CFD runs are shown: a) Newtonian model, b) GPR I viscosity model, c) GPR II viscosity model.

508 In general, contour plots with similar trends were already obtained as a result of simulations of  
 509 different blends with this computational domain. Fig. 14 illustrates the contour plot for viscosity  
 510 in the same plane. Since the Newtonian model was employed, Fig. 14.a reports a constant value,  
 511 and the viscosity corresponds to an intermediate value when compared to the whole interval of  $\mu$

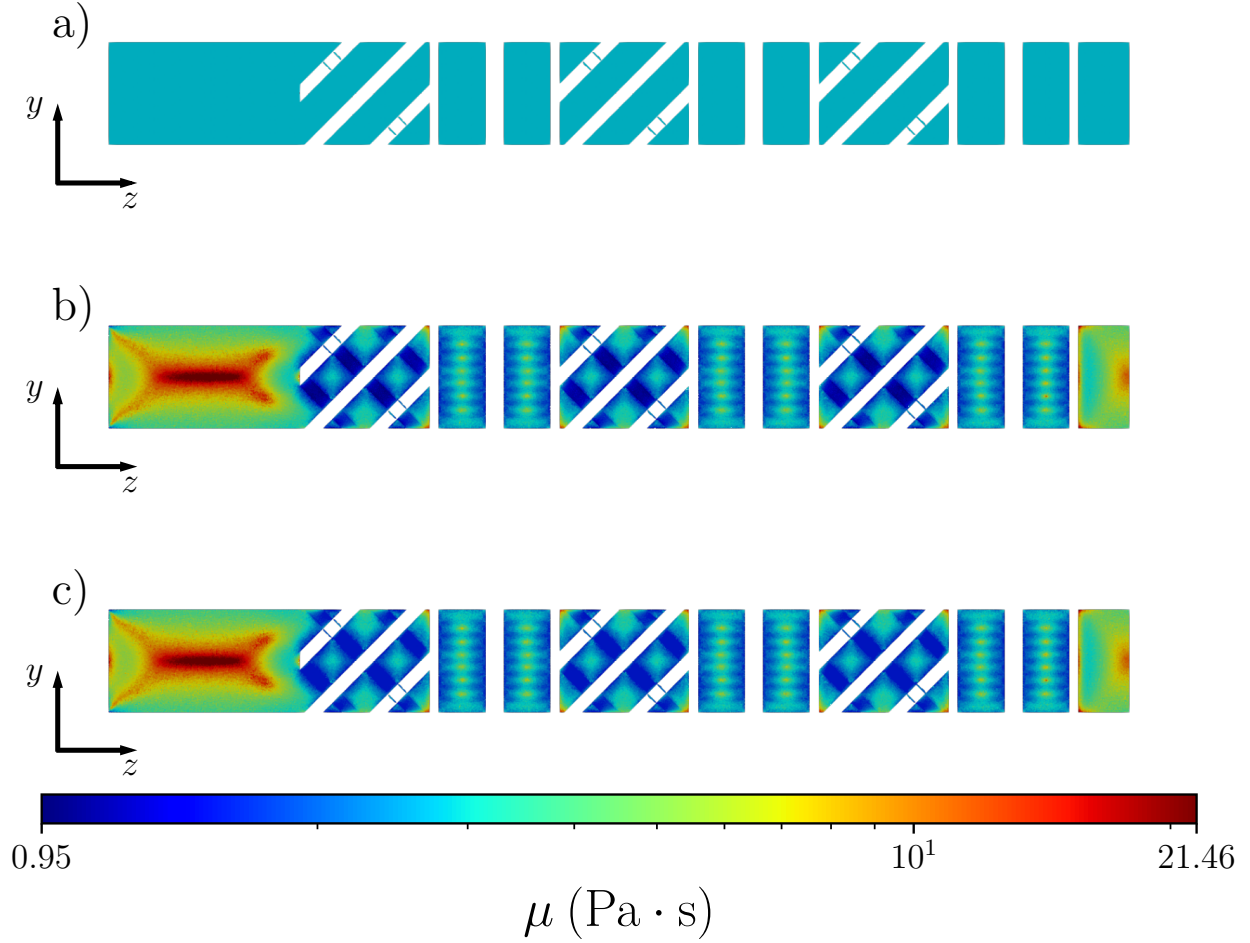


FIG. 14. Contour plot for the viscosity  $\mu$  in correspondence of the slice  $\mathcal{A}$ . The values are plotted using a logarithmic scale for the colorbar. Different CFD runs are shown: a) Newtonian model, b) GPR I viscosity model, c) GPR II viscosity model.

explored by the GPR models. As already noticeable from the rheogram in Fig. 10, the model of a shear-thinning fluid resulted from the DPD simulations. This shear-thinning behavior is visible in Fig. 14.b, where the viscosity is lower in correspondence with the high strain rate regions of the mixing elements (Fig. 13.b).

When compared with the viscosity of the GPR model, the value of  $\mu$  for the Newtonian simulation resulted lower in the inlet and outlet regions, but higher in the mixing section. Since the latter brings a substantially higher contribution to the pressure drop, the Newtonian model presented a value of  $\Delta p$  higher by one order of magnitude than the GPR models, as in Table XI. The difference between GPR I and GPR II can be ascribed to the different  $\dot{\gamma}$  explored: the GPR

TABLE XI. Pressure drop across the static mixer system for the different CFD simulations.

CFD run	$\Delta p$ (Pa)
Newtonian	$2.90 \times 10^5$
GPR I	$2.41 \times 10^4$
GPR II	$2.50 \times 10^4$

I simulation reached higher values of strain rate (Table X), resulting in a lower viscosity in the mixing section and slightly lower  $\Delta p$ . As the final result, the pressure drop obtained from the last CFD simulation was  $\Delta p = 2.50 \times 10^4$  Pa. Though it is not possible to carry a validation of this result, its order of magnitude can be considered reasonable given the investigations done by Solvay in static mixers. In particular, a comparison can be done with a mixture at 65% of SLES in water, flowing in an SMX static mixer with a smaller diameter of  $4.95 \times 10^{-3}$  m. This system has been studied through CFD simulations and with the correlations proposed by Liu, Hrymak, and Wood<sup>34</sup>, using a power law to model its rheology. For a generalized Metzner – Reed Reynolds number<sup>34,54</sup> of  $Re_{MR} = 6.54 \times 10^{-2}$  it was obtained  $\Delta p = 1.66 \times 10^4$  Pa · s from the CFD simulations, and  $\Delta p = 1.70 \times 10^4$  Pa · s using the correlation of Liu, Hrymak, and Wood<sup>34</sup>. By fitting the experimental measures available on Miraspec UB75 (see Section III B 3 with a power law, it was possible to calculate  $Re_{MR} = 6.38 \times 10^{-2}$  for the simulation of this work. The comparisons between these results show an agreement on the order of magnitude, though they cannot be considered as a validation process.

### 3. Viscosity model from DPD simulations

The application of a shear to a DPD fluid still presents some unsolved issues. In particular, an unphysical shear-thickening behaviour was found even for Newtonian fluids in high shear rate conditions<sup>22</sup>. Moreover, for very low shear rate values the thermal noise prevails on the streaming velocity imposed by the box deformation. As a consequence, it becomes impossible to obtain a linear velocity profile, *i. e.* a constant imposed shear rate, and apply Eq. (10). The use of DPD simulations in large shear rate intervals should be tested, to avoid the occurrence of the described computational artifacts. In this work, partial mitigation of these effects was obtained through the use of a higher dissipative DPD constant  $\gamma$  combined with the SLLOD equation of motion.



Therefore, the results used to build the rheology model were obtained from simulations performed in a safe DPD shear rate interval.

The viscosity results obtained from the DPD simulations were compared with the results of two sets of experiments, previously performed at Solvay with the blend Miraspec UB75. The measurements were carried out with the Brookfield DV-II+ viscometer, using the LV3 spindle at 25 °C. The results are shown in Fig. 15, where it is important to remember that the first DPD point corresponds perfectly because this point was used to identify the conversion factor in Table VI. The agreement between the simulations and the experiments is remarkably good, but more simulations and experiments are needed to increase the robustness of the model. In particular, the effect of the temperature and composition should be taken into account since they can have a great impact on the value of viscosity of these kinds of mixtures.

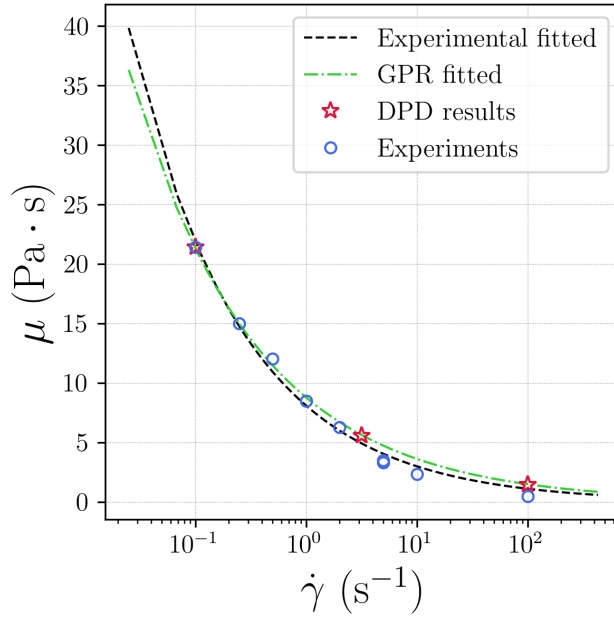


FIG. 15. Comparison between the viscosity model obtained from experimental results and DPD simulations. The blue hollow circles represent the experiments performed at Solvay, and the red hollow stars are the results of the DPD simulations. The black dashed line is the power law resulting from the fitting of the experimental data, while the green dashed and dotted line is the power law resulting from the fitting of one thousand GPR predictions logarithmically spaced on the interval from GPR I in Table X.

To further assess the quality of the viscosity model built on the DPD simulations, a power law, as in Eq. (19), was used to fit both the experimental data and the prediction from the GPR.

$$\mu = m \cdot \dot{\gamma}^{n-1} \quad (19)$$

The power law is one of the most commonly used functions in rheology to approximate the behaviour of shear-thinning fluids for intermediate shear rates. It must be reminded that the GPR does not output a functional form, but a value of apparent viscosity for every value shear rate value in input. Hence, to obtain a power law model for comparison, the GPR was performed to produce one thousand of  $(\dot{\gamma}, \mu)$  couple of points in the final interval (GPR I in Table X). These points are fitted with a power law and the comparison with the power law generated from the experimental data is illustrated in Fig. 15, while the parameters of the power law are reported in Table XII. As it is possible to see from Fig. 15 and Table XII, the two fitted functions are close to each other, indicating that the GPR model provides a physically reasonable description.

TABLE XII. Parameters obtained from the fitting process of the experimental and GPR data using the power law in Eq. (19).

Data set	$m, (\text{Pa} \cdot \text{s}^n)$	$n - 1$
Experimental	$8.11 \pm 3.0 \times 10^{-1}$	$-0.432 \pm 2.0 \times 10^{-2}$
GPR	$8.81 \pm 3.0 \times 10^{-3}$	$-0.383 \pm 1.4 \times 10^{-4}$

#### 4. Multiscale approach computational performance

The idea behind the approach described in this work is the automatic selection of which DPD simulation to perform. This should lead to a reduction of the computational resources needed, through the minimization of the number of DPD simulations. The simulations were performed on a workstation with a CPU “Intel® Xeon® Gold 6248 CPU @ 3.00GHz” using 24 cores. The time requested by each simulation is reported in Table XIII. Here the CFD simulations are identified through the viscosity model used to perform them, while the DPD simulations are numbered following the order of execution. It is possible to discriminate between these DPD simulations through the applied shear rate, as reported in Table XIV. In Table XIII is, instead, evident that the DPD simulations are the bottleneck of the automated approach, requesting from six to ten times the time of a CFD simulation.

For what concerns the variability of the time needed to complete a simulation, it looks that a simulation with the GPR model can take up to four times more time than a Newtonian one. Actually, the Newtonian simulation stopped after 588 iterations, while the GPR model continued until

TABLE XIII. List of simulations in the order in which they were performed, with the corresponding computational time. The performed *inner loops* are also indicated.

	Simulation	Computational time (h:m)
1° GPR–DPD loop	CFD Newtonian	0:14
	DPD 1°	6:08
	DPD 2°	11:24
	DPD 3°	8:02
	CFD GPR I	1:09
	CFD GPR II	1:10

2000 iterations. This can be the sign of too strict convergence criteria for the CFD simulation, which can be affected not only by the viscosity model but also by the quality of the mesh. Consequently, a different mesh or a better choice of the convergence parameter could lead to a reduction of the computational time.

TABLE XIV. List of DPD simulations with the corresponding time to completion and the imposed shear rate  $\dot{\gamma}$ . The simulations are ordered with increasing  $\dot{\gamma}$ , to highlight the dependence of the requested time on the imposed shear rate.

Simulation	$\dot{\gamma}$ (DPD units)	Computational time (h:m)
DPD 1°	0.01	6:08
DPD 3°	0.317	8:02
DPD 2°	10	11:24

Conversely, for the DPD simulation, there is a strong dependence of the computational time on the value of  $\dot{\gamma}$ . Higher values of the shear rate imposed on the simulation box lead to longer computational times to complete the simulation, according to Table XIII.

Using an automated approach for choosing the best shear rate value to add a point to the training data set led to satisfactory results in terms of computational time. Nonetheless, it must be noted that the rheogram resulted simple enough to obtain a good quality regression with only three training points. Consequently, to assess the computational advantages of this approach with more accuracy, it should be tested on a more complex rheology model, *e.g.* including the effect of

composition. Instead, for what concerns the CFD and DPD techniques, the computational time depends strongly on the models implemented in these kinds of simulations, so it is not possible to make a generalization.

#### IV. CONCLUSIONS

The main purpose of the work was to develop a multiscale automated approach that could allow the simulation of fluids in a typical mixing piece of equipment. The macroscale Computational Fluid Dynamics (CFD) simulations are used to get information on macroscopic variables, such as the pressure drops across a static mixer. The mesoscale Dissipative Particle Dynamics (DPD) simulations are instead used to build a rheology model for the non-Newtonian fluid of interest. In order to reduce the computational resources needed for the simulations, the Gaussian Process Regression (GPR) was used to build the rheological model from the DPD non-equilibrium simulations.

The fluid of interest, the blend Miraspec UB75, was modelled using a parametrization developed for similar surfactants. Using this parametrization, a part of the phase diagram of a mixture of SLES and water was successfully reproduced from a qualitative point of view. This confirmed the capabilities of the DPD technique to obtain qualitative information about the microstructure of the simulated fluids. Non-equilibrium simulations were used to reproduce the rheological behaviour of the fluid under the application of shear stress. The application of the shear condition on the simulation box showed some limitations of the DPD method, regarding the explorable shear rates. It was noticed that for too high or too low values of  $\dot{\gamma}$ , the results of the non-equilibrium simulations are less reliable. This is common to all atomistic methods, but it would be beneficial to study how to mitigate the effects of extreme strain rate conditions on the quality of the predictions. Despite this issue, it was possible to reproduce the rheological behaviour of the studied fluid. The obtained  $\Delta p$  were realistic when compared to the behavior of similar blends in the same mixing devices. Moreover, the value of viscosity obtained with the DPD simulation resulted in remarkably good agreement with two sets of experiments conducted at different shear rates. This is noteworthy in light of the approach used for the identification of the conversion factors, which is often a weak point in non-equilibrium DPD simulations. Indeed, deriving the conversion factor by matching the value of viscosity for the lowest applicable shear rate led to promising results.

To conclude, this work shows the feasibility of an automated multiscale approach to describe a

real system that is relatively simple in terms of chemical composition, but further studies should be conducted to explore the limits of the DPD technique. Among these, the more critical are the parametrization of the molecules and the description of local charges, the width of the explorable shear rate interval in non-equilibrium simulations, and the possibility of simulation for non-isothermal systems. Furthermore, an experimental campaign could allow a more robust validation of the developed model.

## ACKNOWLEDGMENTS

The authors gratefully acknowledge Dr. Richard Anderson for his insights and for providing the missing parameters of the model. This research is partially financially supported by ICSC – Centro Nazionale di Ricerca in High Performance Computing, Big Data and Quantum Computing, funded by European Union – NextGenerationEU. Financial support also comes from the Italian Ministry of University and Research via the PRIN project (Project number: 2022JJRH8H; Project name: Non-equilibrium self-assembly of structured fluids: a multi-scale engineering problem. Computational resources were provided by HPC@POLITO, a project of Academic Computing within the Department of Control and Computer Engineering at the Politecnico di Torino (<http://www.hpc.polito.it>). We acknowledge the CINECA award under the ISCRA initiative, for the availability of high performance computing resources and support.

## REFERENCES

- <sup>1</sup>K. Klein and I. Palefsky, “C.2 - Shampoo Formulation,” in *Handbook for Cleaning/Decontamination of Surfaces*, edited by I. Johansson and P. Somasundaran (Elsevier Science B.V., Amsterdam, 2007) pp. 277–304.
- <sup>2</sup>N. Pandya, G. Rajput, D. S. Janni, G. Subramanyam, D. Ray, V. Aswal, and D. Varade, “SLES/CMEA mixed surfactant system: Effect of electrolyte on interfacial behavior and microstructures in aqueous media,” *Journal of Molecular Liquids* **325**, 115096 (2021).
- <sup>3</sup>H. Li, L. Dang, S. Yang, J. Li, and H. Wei, “The study of phase behavior and rheological properties of lyotropic liquid crystals in the LAS/AES/H<sub>2</sub>O system,” *Colloids and Surfaces A: Physicochemical and Engineering Aspects* **495**, 221–228 (2016).
- <sup>4</sup>R. I. Castaldo, R. Pasquino, M. M. Villone, S. Caserta, C. Gu, N. Grizzuti, S. Guido, P. L.

- Maffettone, and V. Guida, “Dissolution of concentrated surfactant solutions: From microscopy imaging to rheological measurements through numerical simulations,” *Soft Matter* **15**, 8352–8360 (2019).
- <sup>5</sup>A. Capaccio, S. Caserta, S. Guido, G. Rusciano, and A. Sasso, “Dissolution of a surfactant-water lamellar phase investigated by combining time-lapse polarized light microscopy and confocal Raman spectroscopy,” *Journal of Colloid and Interface Science* **561**, 136–146 (2020).
- <sup>6</sup>G. E. Son, N. Sugartseren, W.-B. Yoon, and S. K. Kwak, “Phase Behavior of Ternary Mixtures of Water–Vanillin–Ethanol for Vanillin Extraction via Dissipative Particle Dynamics,” *Journal of Chemical & Engineering Data* **59**, 3036–3040 (2014).
- <sup>7</sup>H. Droghetti, I. Pagonabarraga, P. Carbone, P. Asinari, and D. Marchisio, “Dissipative particle dynamics simulations of tri-block co-polymer and water: Phase diagram validation and microstructure identification,” *The Journal of Chemical Physics* **149**, 184903 (2018).
- <sup>8</sup>R. D. Groot and P. B. Warren, “Dissipative particle dynamics: Bridging the gap between atomistic and mesoscopic simulation,” *The Journal of Chemical Physics* **107**, 4423–4435 (1997).
- <sup>9</sup>S.-L. Yuan, Z.-T. Cai, G.-Y. Xu, and Y.-S. Jiang, “Mesoscopic simulation study on phase diagram of the system oil/water/aerosol OT,” *Chemical Physics Letters* **365**, 347–353 (2002).
- <sup>10</sup>A. Prhashanna, S. A. Khan, and S. B. Chen, “Co-Micellization Behavior in Poloxamers: Dissipative Particle Dynamics Study,” *The Journal of Physical Chemistry B* **119**, 572–582 (2015).
- <sup>11</sup>J. G. E. M. Fraaije, J. van Male, P. Becherer, and R. Serral Gracià, “Coarse-Grained Models for Automated Fragmentation and Parametrization of Molecular Databases,” *Journal of Chemical Information and Modeling* **56**, 2361–2377 (2016).
- <sup>12</sup>M. Ferrari, J.-W. Handgraaf, G. Boccardo, A. Buffo, M. Vanni, and D. L. Marchisio, “Molecular modeling of the interface of an egg yolk protein-based emulsion,” *Physics of Fluids* **34**, 021903 (2022).
- <sup>13</sup>M. Ferrari, G. Boccardo, D. L. Marchisio, and A. Buffo, “Application of dissipative particle dynamics to interfacial systems: Parameterization and scaling,” *AIP Advances* **13**, 035324 (2023).
- <sup>14</sup>R. L. Anderson, D. J. Bray, A. S. Ferrante, M. G. Noro, I. P. Stott, and P. B. Warren, “Dissipative particle dynamics: Systematic parametrization using water-octanol partition coefficients,” *The Journal of Chemical Physics* **147**, 094503 (2017).
- <sup>15</sup>M. Panoukidou, C. R. Wand, A. Del Regno, R. L. Anderson, and P. Carbone, “Constructing the phase diagram of sodium laurylthoxysulfate using dissipative particle dynamics,” *Journal of Colloid and Interface Science* **557**, 34–44 (2019).

- <sup>16</sup>R. L. Anderson, D. J. Bray, A. Del Regno, M. A. Seaton, A. S. Ferrante, and P. B. Warren, “Micelle Formation in Alkyl Sulfate Surfactants Using Dissipative Particle Dynamics,” [Journal of Chemical Theory and Computation](#) **14**, 2633–2643 (2018).
- <sup>17</sup>A. Del Regno, P. B. Warren, D. J. Bray, and R. L. Anderson, “Critical Micelle Concentrations in Surfactant Mixtures and Blends by Simulation,” [The Journal of Physical Chemistry B](#) **125**, 5983–5990 (2021).
- <sup>18</sup>C. R. Wand, M. Panoukidou, A. Del Regno, R. L. Anderson, and P. Carbone, “The Relationship between Wormlike Micelle Scission Free Energy and Micellar Composition: The Case of Sodium Lauryl Ether Sulfate and Cocamidopropyl Betaine,” [Langmuir](#) **36**, 12288–12298 (2020).
- <sup>19</sup>E. S. Boek, P. V. Coveney, and H. N. W. Lekkerkerker, “Computer simulation of rheological phenomena in dense colloidal suspensions with dissipative particle dynamics,” [Journal of Physics: Condensed Matter](#) **8**, 9509 (1996).
- <sup>20</sup>E. S. Boek, P. V. Coveney, H. N. W. Lekkerkerker, and P. van der Schoot, “Simulating the rheology of dense colloidal suspensions using dissipative particle dynamics,” [Physical Review E](#) **55**, 3124–3133 (1997).
- <sup>21</sup>Y. Kong, C. Manke, W. Madden, and A. Schlijper, “Modeling the rheology of polymer solutions by dissipative particle dynamics,” [Tribology Letters](#) **3**, 133–138 (1997).
- <sup>22</sup>A. Boromand, S. Jamali, and J. M. Maia, “Viscosity measurement techniques in Dissipative Particle Dynamics,” [Computer Physics Communications](#) **196**, 149–160 (2015).
- <sup>23</sup>N. Lauriello, J. Kondracki, A. Buffo, G. Boccardo, M. Bouaifi, M. Lisal, and D. Marchisio, “Simulation of high Schmidt number fluids with dissipative particle dynamics: Parameter identification and robust viscosity evaluation,” [Physics of Fluids](#) **33**, 073106 (2021).
- <sup>24</sup>N. Lauriello, G. Boccardo, D. Marchisio, M. Lisal, and A. Buffo, “Development of an automated reliable method to compute transport properties from DPD equilibrium simulations: Application to simple fluids,” [Computer Physics Communications](#) **291**, 108843 (2023).
- <sup>25</sup>A. Prhashanna, S. A. Khan, and S. B. Chen, “Micelle morphology and chain conformation of triblock copolymers under shear: LA-DPD study,” [Colloids and Surfaces A: Physicochemical and Engineering Aspects](#) **506**, 457–466 (2016).
- <sup>26</sup>K. P. Santo, A. Vishnyakov, R. Kumar, and A. V. Neimark, “Elucidating the Effects of Metal Complexation on Morphological and Rheological Properties of Polymer Solutions by a Dissipative Particle Dynamics Model,” [Macromolecules](#) **51**, 4987–5000 (2018).
- <sup>27</sup>M. H. Nafar Sefiddashti, M. Boudaghi-Khajehnobar, B. J. Edwards, and B. Khomami, “High-

fidelity scaling relationships for determining dissipative particle dynamics parameters from atomistic molecular dynamics simulations of polymeric liquids,” [Scientific Reports](#) **10**, 4458 (2020).

<sup>28</sup>S. Meng, J. Zhang, Y. Wang, X. Li, C. Wu, T. Hou, L. Xiao, and G. Lu, “Simulating the rheology of surfactant solution using dissipative particle dynamics,” [Molecular Simulation](#) **41**, 772–778 (2015).

<sup>29</sup>C. Junghans, M. Praprotnik, and K. Kremer, “Transport properties controlled by a thermostat: An extended dissipative particle dynamics thermostat,” [Soft Matter](#) **4**, 156–161 (2007).

<sup>30</sup>C. P. Lowe, “An alternative approach to dissipative particle dynamics,” [Europhysics Letters](#) **47**, 145 (1999).

<sup>31</sup>S. D. Stoyanov and R. D. Groot, “From molecular dynamics to hydrodynamics: A novel Galilean invariant thermostat,” [The Journal of Chemical Physics](#) **122**, 114112 (2005).

<sup>32</sup>M. Coroneo, G. Montante, A. Paglianti, and F. Magelli, “CFD prediction of fluid flow and mixing in stirred tanks: Numerical issues about the RANS simulations,” [Computers & Chemical Engineering](#) **35**, 1959–1968 (2011).

<sup>33</sup>M. Ferrari, G. Boccardo, A. Buffo, M. Vanni, and D. L. Marchisio, “CFD simulation of a high-shear mixer for food emulsion production,” [Journal of Food Engineering](#) **358**, 111655 (2023).

<sup>34</sup>S. Liu, A. N. Hrymak, and P. E. Wood, “Laminar mixing of shear thinning fluids in a SMX static mixer,” [Chemical Engineering Science](#) **61**, 1753–1759 (2006).

<sup>35</sup>P. Pianko-Oprych and Z. Jaworski, “CFD modelling of two-phase liquid-liquid flow in a SMX static mixer,” [Polish Journal of Chemical Technology](#) **11**, 41–49 (2009).

<sup>36</sup>B. W. Nyande, K. Mathew Thomas, and R. Lakerveld, “CFD Analysis of a Kenics Static Mixer with a Low Pressure Drop under Laminar Flow Conditions,” [Industrial & Engineering Chemistry Research](#) **60**, 5264–5277 (2021).

<sup>37</sup>L. Zhao, Z. Li, B. Caswell, J. Ouyang, and G. E. Karniadakis, “Active learning of constitutive relation from mesoscopic dynamics for macroscopic modeling of non-Newtonian flows,” [Journal of Computational Physics](#) **363**, 116–127 (2018).

<sup>38</sup>L. Zhao, Z. Li, Z. Wang, B. Caswell, J. Ouyang, and G. E. Karniadakis, “Active- and transfer-learning applied to microscale-macroscale coupling to simulate viscoelastic flows,” [Journal of Computational Physics](#) **427**, 110069 (2021).

<sup>39</sup>P. J. Hoogerbrugge and J. M. V. A. Koelman, “Simulating microscopic hydrodynamic phenomena with dissipative particle dynamics,” [Europhysics Letters \(EPL\)](#) **19**, 155–160 (1992).



- <sup>40</sup>P. Español and P. Warren, “Statistical mechanics of dissipative particle dynamics,” *Europhysics Letters (EPL)* **30**, 191–196 (1995).
- <sup>41</sup>P. Español and P. B. Warren, “Perspective: Dissipative particle dynamics,” *The Journal of Chemical Physics* **146**, 150901 (2017).
- <sup>42</sup>A. W. Lees and S. F. Edwards, “The computer study of transport processes under extreme conditions,” *Journal of Physics C: Solid State Physics* **5**, 1921–1928 (1972).
- <sup>43</sup>A. P. Thompson, H. M. Aktulga, R. Berger, D. S. Bolintineanu, W. M. Brown, P. S. Crozier, P. J. in ’t Veld, A. Kohlmeyer, S. G. Moore, T. D. Nguyen, R. Shan, M. J. Stevens, J. Tranchida, C. Trott, and S. J. Plimpton, “LAMMPS - a flexible simulation tool for particle-based materials modeling at the atomic, meso, and continuum scales,” *Computer Physics Communications* **271**, 108171 (2022).
- <sup>44</sup>D. J. Evans and G. P. Morriss, *Statistical Mechanics of Nonequilibrium Liquids* (ANU Press, 2007).
- <sup>45</sup>B. D. Todd and P. J. Daivis, *Nonequilibrium Molecular Dynamics: Theory, Algorithms and Applications* (Cambridge University Press, Cambridge, 2017).
- <sup>46</sup>Y. Koide and S. Goto, “Effect of scission on alignment of nonionic surfactant micelles under shear flow,” *Soft Matter* **19**, 4323–4332 (2023).
- <sup>47</sup>R. D. Groot, “Electrostatic interactions in dissipative particle dynamics—simulation of polyelectrolytes and anionic surfactants,” *The Journal of Chemical Physics* **118**, 11265–11277 (2003).
- <sup>48</sup>M. González-Melchor, E. Mayoral, M. E. Velázquez, and J. Alejandre, “Electrostatic interactions in dissipative particle dynamics using the Ewald sums,” *The Journal of Chemical Physics* **125**, 224107 (2006).
- <sup>49</sup>C. E. Rasmussen and C. K. I. Williams, *Gaussian Processes for Machine Learning* (2005).
- <sup>50</sup>F. Pedregosa, G. Varoquaux, A. Gramfort, V. Michel, B. Thirion, O. Grisel, M. Blondel, P. Prettenhofer, R. Weiss, V. Dubourg, J. Vanderplas, A. Passos, D. Cournapeau, M. Brucher, M. Perrot, and É. Duchesnay, “Scikit-learn: Machine Learning in Python,” *Journal of Machine Learning Research* **12**, 2825–2830 (2011).
- <sup>51</sup>J. Fink, “*Gaussian Process Library*,” (2015).
- <sup>52</sup>J. Sossa-Echeverria and F. Taghipour, “Computational simulation of mixing flow of shear thinning non-Newtonian fluids with various impellers in a stirred tank,” *Chemical Engineering and Processing: Process Intensification* **93**, 66–78 (2015).
- <sup>53</sup>OpenFOAM Foundation, “OpenFOAM - The Open Source CFD Toolbox,” <https://www.>

778 [openfoam.com/](https://openfoam.com/) (2020), version 8.0.

779 <sup>54</sup>A. B. Metzner and J. C. Reed, “Flow of non-newtonian fluids—correlation of the laminar, tran-  
780 sition, and turbulent-flow regions,” [AIChE Journal](#) **1**, 434–440 (1955).